Reduced Simulations: A New Technique for $\gamma - \gamma$ Angular Correlation Analysis

—————————————————

A Thesis

Presented to

The Division of Mathematics and Natural Sciences

Reed College

—————————————————

In Partial Fulfillment

of the Requirements for the Degree

Bachelor of Arts

—————————————————

William H. Ashfield IV

May 2017

Approved for the Division
(Physics)

Jenna K. Smith

Acknowledgements

It goes without saying that the institution that is Reed College is something of an anomaly. It is[1] iconoclastic by design, and subjects its students to arguably unnecessary amounts of pressure and stress, both socially and academically. By pushing us to our limits, it manages to teach us something about ourselves, something about our community, something more in addition to whatever each of us came here to learn in the first place. For better and for worse this college has left a permanent mark on who I am. And I have to acknowledge that at least.

That being said, I have to begin by thanking Jenna for being the best advisor in the department. Your patience with my stupidity at times was more than appreciated, and I am happy to have chosen this project. I learned so much. River, Oskar, Mikaela, Max, Lucas - we were friends from day one, and I hold you all close to my heart. Special shout out to Edgar, Gabe, Elias, Kaustuv, Keppler, and Rohan. I love the shit out of you guys. To my two cats, Stevie and Nixon too. Alex, thank you for being there when I needed you time and time again. You truly helped me in so many ways, and I will always love our time here together. Annie, I cannot believe the person you are turning into. Watching your life unfold is going to be a highlight of my own. To those I left out and to those reading this, I love you too.

Most importantly, none of this would have been possible without my Mom. The sacrifices you made have put me where I am today, and I just want you to know that is wasn't for nothing. This one is for you.

---

[1]was

Table of Contents

List of Tables

List of Figures

Abstract

The Reduced Simulations method was developed as a data analysis technique for $\gamma - \gamma$ angular correlations. By defining and implementing the $\mathcal{Z}$ distribution - a linear combination of simulated Legendre polynomials - it was shown that simulated angular correlation data could be recreated for any spin cascade of a ^{60}Co decay. Consequently, goodness-of-fit tests performed between simulated data and the $\mathcal{Z}$ distribution were able to reproduce previous results assigning spins to excited nuclear level states with a dramatic reduction in computational cost. In addition, the $\mathcal{Z}$ distribution was approximated to produce a set of algebraic expressions capable of correcting the detector effects found in the angular correlation coefficients measured in simulation or experiment, allowing for a goodness-of-fit test to be reproduced analytically.

Introduction

This thesis focuses on nuclear physics, and the measurement of γ rays emitted from nuclear decay in particular. In order to become oriented with the nature of the reactions caused by the interactions of protons and neutrons, it is often helpful to begin with a familiar system: the Bohr model of the atom.

Given the Bohr model for hydrogen[2], there exists an electron orbiting a proton at a certain energy. If left undisturbed, this electron will continue to orbit the proton stably, without radiating energy, for an infinite amount of time. However, the electron can move to higher or lower energy states by either emitting or absorbing a photon at an energy equal to the difference in energy of the two states: $E_\gamma = E_2 - E_1$. Here, Bohr was able to show the energy states of electrons were quantized, as the angular momentum of the electron could only exist in integer multiples of $\hbar$: $L_{e^-} = n\hbar$. Additionally, the absorbed or emitted photon that allowed for energy transitions was shown to carry the difference in angular momentum between two states. A nucleus, like an atom, exhibits similar properties.

There are currently 115 known elements, each having its own particular number of protons (known as the atomic number Z). For each element, a number of different isotopes can exist, where the number of neutrons in the nucleus varies, but the number of protons remains the same. 80 elements are known to have at least one stable isotope, with a total of 254 stable isotopes known [7]. The thousands of isotopes that are not stable decay in various was to change the number of protons or neutrons found in the atom in an attempt to reach stability. If the atomic number Z is plotted against number of neutrons for a number of nuclei, the stability of different isotopes can be easily seen. This plot is shown in Figure 1, and is called the chart of nuclides. Here, each color represents the lifetime of an isotope, with the black squares showing the 254 stable nuclei.

After an isotope decays into a different, more stable nucleus, it could end up in an excited energy state. Just like an atom, a nucleus in an excited state will decay into

---

[2]It is understood that the Bohr model is an incorrect, yet simple atomic model.
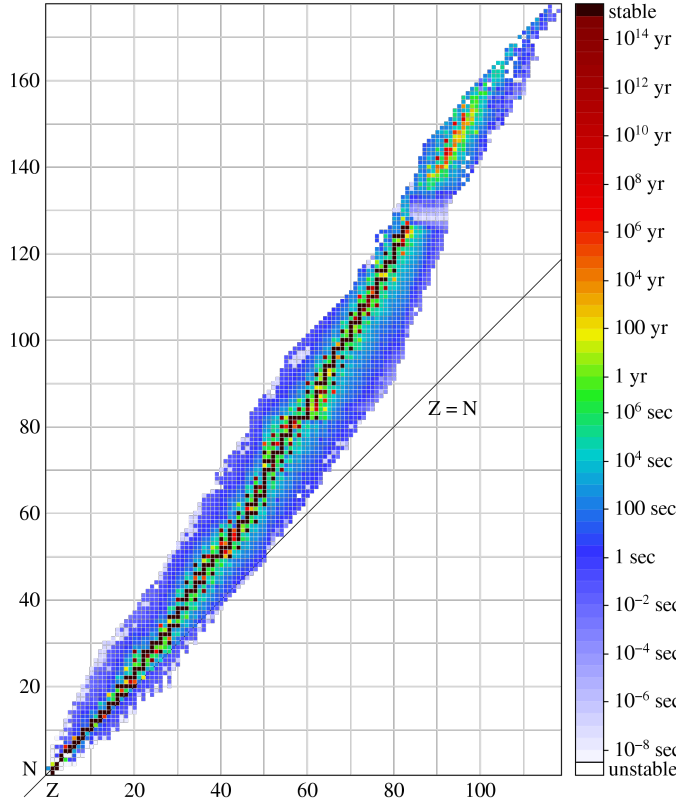
Figure 1: The chart of nuclides, with number of protons against the number of neutrons. Color indicates lifetime of isotope. [2].

a lower state by emitting a photon, or γ ray, with an energy equal to the difference in energies between the states. In addition to quantized states, a nucleus also exhibits angular momentum properties.

Like any quantum mechanical system, the orbital angular momentum $\mathbf{l}$ and spin $\mathbf{s}$ couple to give the total angular momentum, $\mathbf{j}$:

$$\mathbf{j} = \mathbf{l} + \mathbf{s}, \tag{1}$$

which behaves similarly to l and s:

$$\langle \mathbf{j}^2 \rangle = \hbar^2 j(j+1)$$
$$\langle j_z \rangle = \langle l_z + s_z \rangle = \hbar m_j. \tag{2}$$

Here, m_j is the magnetic substate of the total angular momentum and is constrained between $-j$ and j in integer steps[8]. For any a given nucleus, we can describe each nucleon with the quantum numbers j, l, and s. The total angular momentum of

a nucleus containing A nucleons is then the vector sum of the angular momenta of all nucleons. This quantity is normally called the *nuclear spin*, $\mathbf{J}$, and it shares the usual properties of quantum angular momentum vectors seen in Equations 1.1 and 1.2. In most circumstances, a nucleus behaves as if it were a single, spinning particle with spin $\mathbf{J}$ and spin quantum number J, which is why these quantities are used to describe nuclear states.

As an aside, because J is composed of all z components of the individual nucleons there are restrictions on values that J can take. Each individual j must be half-integral, as the spin of nucleons are $\frac{1}{2}$ and the orbital angular momentum is always an integer. Hence, if there is an odd number of nucleons in a nucleus, the spin will be half-integral. Conversely, if a nucleus has an even number of nucleons, the spin will be an integer.

In addition to nuclear spin, parity, π is also used to characterize nuclear states. The parity operation is responsible for a total reflection through an origin, $\mathbf{r} \to -\mathbf{r}$, where the case $\psi(-\mathbf{r}) = +\psi(\mathbf{r})$ is even parity and the case $\psi(-\mathbf{r}) = -\psi(\mathbf{r})$ is odd parity. For a system of many particles, the wave function for the entire system is formed from the product of the wave functions for the individual particles. Therefore, a nuclear state has a definite odd or even parity, which is often denoted as a + or - superscript on the nuclear spin: $\mathbf{J}^{\pi}$ [3].

For the γ-ray decay of a nucleus, the emitted photon must carry away the energy, angular momentum, and parity differences between the two nuclear states. In a process that is further described in the following chapter, the distribution of emitted photons from a radioactive source can be made to be anisotropic using a technique known as angular correlation. By measuring the angular distribution between the photons in space, it becomes possible to measure and assign the spins and parities of these states, and advance the understanding of nuclear structure.

---

[3]It is important to note that any spin $\mathbf{J}$ can theoretically have either $\pi = +$ or $\pi = $ -.

Chapter 1

Theory

In this chapter, the physical theories behind $\gamma - \gamma$ angular correlations are discussed. First, the basic concepts of nuclear radiation in general are explain before the specifics of γ decay and its approximation as a classical radiation field are considered. Sections 1.1 and 1.2 are meant as a supplement to understanding how γ rays are emitted in space and how angular correlations are measured. It should be noted here that the material covered below is built from a classical understanding of nuclear radiation, that brings in a few quantum mechanical elements when appropriate. In order to better comprehend γ decay, a more robust understanding of quantum mechanics is preferable. For more advanced readers, a good supplement to this chapter can be found in *Nuclear Physics in a Nutshell* by Carlos Bertulani [9].

1.1 Radioactive Decay

Nuclei that are unstable or are in an excited state will emit radiation in order to achieve stability. The four main decay processes common for a nucleus are nuclear fission, as well as α, β, and γ decay. Notably seen in heavier nuclei, spontaneous fission occurs when the nucleus fragments into two large parts and emits free neutrons in the process. Similarly, α decay is the emission of a particle consisting of two protons and two neutrons, or a helium nucleus. With β decay there are two modes: β^- and β^+. β^- decay occurs when a neutron is converted into a proton, emitting an electron and an anti-neutrino in the process. β^+ decay is the reverse process of a proton converting to a neutron, which then emits a positron and a neutrino. These decays

can be written as such:

$$\alpha \text{ decay:} \quad {}^A_Z X \to {}^{A-4}_{Z-2} U + \alpha$$
$$\beta^- \text{ decay:} \quad {}^A_Z X \to {}^A_{Z+1} U + e^- + \bar{\nu}_e \tag{1.1}$$
$$\beta^+ \text{ decay:} \quad {}^A_Z X \to {}^A_{Z-1} U + e^+ + \nu_e,$$

where A is the mass number, Z is the atomic number (or number of protons), X is the parent nucleus, U is the daughter nucleus, $e^-(e^+)$ is an electron(positron), and $\nu_e(\bar{\nu}_e)$ is a neutrino(antineutrino).

Lastly, there is γ decay, in which the nucleus emits a photon. Instead of a change in the species of a nucleus, the decay mode here is associated with the reconfiguration of nucleons to achieve a lower energy state. Because there is no change in the nuclear composition, γ decay is connected to the de-excitation of excited nuclear states. This process has the form of:

$$^A_Z X^*_N \to {}^A_Z X_N + \gamma, \tag{1.2}$$

with the * representing the initial, excited state. Each decay process above requires the energy of the particles in the initial nuclear system to have a larger rest mass energy than the reactants. The difference in mass energy can be denoted by a Q-value:

$$Q = (m_{initial} - m_{final})c^2, \tag{1.3}$$

where m_{final} includes the mass of the radiation particles.

1.1.1   The Radioactive Decay Law

For a given number of initial nuclei in a sample N_0, the number remaining after a time interval dt is given by:

$$dN = -N_0 \lambda dt, \tag{1.4}$$

where λ is the transition rate. By integrating the above equation, the number of nuclei remaining, N, in the sample in a parent nuclei is given by the nuclear decay law:

$$N(t) = N_0 e^{\lambda t}. \tag{1.5}$$

If the nuclear decay of an isotope has multiple modes of radiation then there exists a decay constant for each mode of decay and the total decay constant is then the sum of each decay, $\lambda_T = \sum_{k=1}^n \lambda_k$. The probabilities for the different decays are then

given by the branching ratios of each decay mode:

$$B_k = \frac{\lambda_k}{\lambda_T},$$ (1.6)

which tells you how often each decay mode occurs over all possible types of decay. This quantity is useful in determining if there is a decay mode that is favored and occurs more frequently.

The transition rate between energy states is a well described quantum mechanical process. Given a stationary state, the expectation value of energy is constant in time. This stability can be seen for an energy E, where the uncertainty of the energy is:

$$\Delta E = \sqrt{\langle E^2 \rangle - \langle E \rangle^2},$$ (1.7)

which vanishes as $\langle E^2 \rangle = \langle E \rangle^2$ in a truly stationary state. Hence, the Heisenberg uncertainty principle implies that $\Delta t = \infty$. In order for a transition to be possible, a weak perturbing potential V' must be subjected to the system along with the original central potential V. By including V' and solving the Schrödinger equation for eigenstates, ψ_n, we can find the approximate eigen energies, E_n. Because the approximate values for E_n are roughy equal to those without solving the Schrödinger equation for V', the addition of V' allows for the system to make transition between ψ_n[10].

For a non-stationary energy state, the uncertainty ΔE takes on a non-zero value. This quantity is often referred to as the width, Γ, and is used to compute the lifetime of a state, τ, which is the average time a state exists before transitioning to a lower state[11]. By associating τ with the time interval during which a measurement is taken, Δt, we can estimate that $\tau \approx \hbar/\Gamma$. Knowing τ, it is then possible to find the transition rate of a system, which is inversely related to its lifetime:

$$\lambda = \frac{1}{\tau}.$$ (1.8)

In order to calculate λ from nuclear wave functions, the initial and final wave functions of the approximate stationary states and the interaction potential V' must be known. With these, the calculation of λ leads to Fermi's Golden Rule:

$$\lambda = \frac{2\pi}{\hbar} |V'_{fi}|^2 \rho(E_f).$$ (1.9)

Here, V'_{fi} is the matrix element that connects the initial and final states and is given

by the expectation value $\langle \psi_f \mid V' \mid \psi_i \rangle$, and $\rho(E_f)$ is the density of final states, or the number of available states per unit energy at the final energy. For a large density of states, there are more states that are available for the initial state to transition to, and thus a larger probability and transition rate. Although Fermi's Golden Rule is independent of transition type, its connection to γ decay is discussed in the following section.

1.2 γ Decay Theory

The process of γ decay involves a nucleus in an initial excited state E_i transitioning to a final state E_f via the emission of a photon. Here, the γ ray carries away energy and momentum, with $E_\gamma = pc = \hbar\omega$. Assuming the nucleus is initially at rest, the emitted γ ray will cause the nucleus to recoil to conserve energy and momentum. In this case, the conservation of total energy and momentum give:

$$E_i = E_f + E_\gamma + T_R$$
$$0 = p_\gamma + p_R, \tag{1.10}$$

where T_R is the kinetic recoil of the nucleus. However, due to the relatively large mass of the nucleus, the recoil energy is very small ($T_R \ll \Delta E$) and $E_\gamma \approx E_i - E_f$ with a correction on the order of 10^{-5} [12]. The energetics of γ radiation between nuclear states allow for the formation of level schemes and assignment of energies to excited states.

1.2.1   Radiation Fields

Electromagnetic radiation can be viewed as a classical wave phenomena, or as a quantum mechanical particle. As a nucleus is more appropriately described using quantum theory, the characterization of γ radiation should also be described as such. However, the classical explanation of electromagnetic radiation allows for a more comprehensive understanding of the process of γ decay.

Static charge and current distributions give rise to static electric and magnetic fields. As was discussed in Section 1.1, these distributions in a nucleus can be approximated in terms of multipole moments. If these static distributions become dynamic and begin to vary in time with a oscillatory frequency ω, then a radiation field is produced. Conveniently, a radiation field, similar to a static field can be analyzed in terms of its multipole approximation. Looking at the dipole field, a static electric

dipole is given by $d = qz$ and a static magnetic dipole is given by $\mu = iA$, for q being the electric charge and A being the vector potential. Electromagnetic radiation fields can then be produced by varying the dipole moments in time. If the charges of an electric dipole oscillate along a z-axis, such that $d(t) = qz\cos(\omega t)$, an electric dipole radiation field is produced. Similarly, if the current could fluctuate in a magnetic dipole, then $\mu(t) = iA\cos(\omega t)$ and a magnetic dipole radiation field is produced.

In general, properties for dipole radiation can be expanded to higher orders of multipole radiation. By defining index L, the multipole order is given by 2^L (where $L = 1$ for dipole, $L = 2$ for quadrupole, etc.). For multipole radiation fields, there exist three important characteristics associated with γ de-excitation:

1. Radiated power relative to a specified direction in space is defined by an angular distribution. For 2^L-pole radiation, this distribution is given by the Legendre polynomial $P_{2L}(\cos\theta)$.

2. The power radiated for $\sigma = E$ or M, with E being electric and M being magnetic is:
$$P(\sigma L) = \frac{2(L+1)c}{\epsilon_0 L[(2L+1)!!]^2}\left(\frac{\omega}{c}\right)^{2L+2}[m(\sigma L)]^2, \tag{1.11}$$
where $m(\sigma L)$ is the amplitude of the time time-varying electric or magnetic multipole moment [13].

3. Electric and magnetic dipole fields have opposite parity. The parity of a given radiation field is:
$$\pi(ML) = (-1)^{L+1}$$
$$\pi(EL) = (-1)^L \tag{1.12}$$

In addition to transmitting energy, a classical radiation field also carries angular momentum. Given the power of a radiation field, the rate at which is angular momentum radiated away from a source is always proportional to the power of that field. In terms of quantum theory, this proportionality is conserved only if each photon carries away a discrete amount of angular momentum, $\mathbf{L}_\gamma$. For a γ-ray transition from an initial state J_i to a final state J_f, conservation of angular momentum requires:
$$\mathbf{J_i} = \mathbf{L}_\gamma + \mathbf{J_f}. \tag{1.13}$$

Because of this conservation, the values of L_γ are restricted between $J_i + J_f$ and $\mid J_i - J_f \mid$. Moreover, since the photon has an intrinsic spin of one, transitions

with $L_\gamma = 0$ are forbidden and thus $J_i = 0 \rightarrow J_f = 0$ cannot occur. The angular momentum of a given state must also be oriented in space, which gives rise to specific magnetic substates m_j. These substates span from $-J$ to J in integer steps, and have units of $\hbar$ [12].

In terms of the multipole expansions for radiation, it can be shown that the angular momentum carried away by the photon is described by the multipole order given by the index L, such that $L_\gamma = L\hbar$ [1]. In turn, the limitations on the values for the angular momentum carried away by a photon are exactly the same for the limitations on the values of index L, effectively restricting the allowed orders of multipole radiation present in a given transition.

Furthermore, the parity of the emitted radiation is determined by the parities of the initial and final states. A change in parity between the states gives a radiation field with odd parity, while no change in parity gives a radiation field with even parity [12]. For either case, parity is always conserved. In reference to Equation 1.12, electric and magnetic multipoles always have opposite parities for any index L, and so the parities of multipolarity for a given transition must alternate as the order increases. Assume that $\pi_i = \pi_f$. In that case, there is no change in parity and the radiation field emitted must be even. Hence, the $L = 1$ must be magnetic as only even parities produce magnetic multipoles for $L =$ odd. The next multipole order, $L = 2$, must then be electric following the same logic. This pattern repeats for a transition with no parity change, where the radiation field is $M1, E2, M3$, and $E4$, for $L = 1, 2, 3$, and 4. In contrast, a change in parity for a transition would produce the opposite: $E1, M2, E3, M4$.

The restrictions on the values of L and π give rise to the following selection rules:

1. $\mid J_i - J_f \mid \leq L \leq J_i + J_f$

2. $\Delta\pi =$ no: even electric, odd magnetic

3. $\Delta\pi =$ yes: odd electric, even magnetic

1.2.2   Weisskopf Estimates and the Mixing Ratio

Classically, the source of a radiation field arises from the time varying multipole moment, $m(\sigma L)$ (Equation 1.11). Quantum mechanically, we can describe the same

---

[1]A detailed analysis shows that multipole index, L, represents the angular momentum quantum number found in the spherical harmonics portion of the quantum-electrodynamic solution to the various nuclear wave functions [9]

multipole moment as an operator that changes nuclear states from ψ_i to ψ_f, while creating an appropriate transitional photon. As mentioned above for Fermi's Golden Rule, the transition rate for a system is determined in part by the matrix element which connects the initial and final states. Therefore, the matrix element for γ decay is defined by the multipole operator:

$$m_{fi}(\sigma L) = \langle \psi_f \mid m(\sigma L) \mid \psi_i \rangle. \tag{1.14}$$

As power is defined to be energy per unit time, dividing Equation 1.11 by the energy of a photon, $\hbar\omega$, gives the transition rate for a γ ray:

$$\lambda(\sigma L) = \frac{P(\sigma L)}{\hbar\omega} = \frac{2(L+1)}{\hbar\epsilon_0 L[(2L+1)!!]^2} \left(\frac{\omega}{c}\right)^{2L+1} [m_{fi}(\sigma L)]^2. \tag{1.15}$$

This equation simplifies if the assumption is made that a transition between states is facilitated by a single photon. Here, the wave function can be separated into radial and angular components. By including an assumption of the radial component being constant out to the nuclear radius and zero outside thereof, the simplified electric and magnetic transitions are then given by:

$$\lambda(EL) = \frac{2\pi\alpha c(L+1)}{L[(2L+1)!!]^2} \left(\frac{E_\gamma}{\hbar c}\right)^{2L+1} \left(\frac{3}{L+3}\right) R^{2L} \tag{1.16}$$

$$\lambda(ML) = \frac{10\alpha c(L+1)}{L[(2L+1)!!]^2} \left(\frac{E_\gamma}{\hbar c}\right)^{2L+1} \left(\frac{3}{L+3}\right) R^{2L-2} \left(\frac{\hbar c}{m_p c^2}\right)^2, \tag{1.17}$$

for $R = R_0 A^{1/3}$ [2], α being the fine structure constant, and m_p being the mass of the the proton [11].

The simplifications for the transmission rates of γ decay calculate what are known as Weisskopf estimates, shown in Table 1.1. By comparing these estimated rates to one another, they provide information about the transmission probabilities. If the atomic mass is taken to be $A \approx 100$ nucleons, then for given multipoles orders L and $L+1$ the estimates show that:

$$\frac{\lambda(\sigma(L+1))}{\lambda(\sigma L)} \approx 10^{-5} E_\gamma^2. \tag{1.18}$$

This result shows that lower multipole orders dominate and are much more likely to occur than their higher order counterparts. Additionally, for a given L the ratio

---

[2] $R_0 \approx 1.2$ fm [11]

Multipole Order	Electric	Magnetic
1	$1.0 \times 10^{14} A^{2/3} E_\gamma^3$	$5.6 \times 10^{13} E^3$
2	$7.3 \times 10^7 A^{4/3} E_\gamma^5$	$3.5 \times 10^7 A^{2/3} E^7$

Table 1.1: Weisskopf estimates for the first two electric and magnetic multipole orders [1].

between electric and magnetic transitions is:

$$\frac{\lambda(EL)}{\lambda(ML)} \approx 10^2 A^{2/3}. \tag{1.19}$$

Although this is a hypothetical comparison, it demonstrates the favoring of electric transitions.

In the event of a of transition where the parity does not change, it is possible for the magnetic transitions of order L to compete with the the electric transitions of order $L+1$, due to the fact that both lower order and electric multipole transitions are favored. For a transition where there is more than one available multipolarity allowed as defined by the selection rules, a combination of electric and magnetic transitions are possible. This is called mixing, and the *mixing ratio* is defined to be:

$$\delta \equiv \frac{\langle \psi_f \mid EL' \mid \psi_i \rangle}{\langle \psi_f \mid ML \mid \psi_i \rangle}, \tag{1.20}$$

for $L' = L + 1$. The individual contributions for a mixed transition are:

$$\begin{aligned} EL' &= \frac{\delta^2}{1 + \delta^2} \\ ML &= \frac{1}{1 + \delta^2}, \end{aligned} \tag{1.21}$$

where $EL' + ML = 1$. Again, these are only estimates for a simple transition between nuclear states, and it is possible for emitted γ rays to act outside this behavior.

1.3   Angular Correlations

In order to experimentally determine the multipole properties of transition radiation it is necessary to take angular distribution measurements of the γ radiation, as energy measurements only limit the possible values of nuclear spin at best. As was discussed in Section 1.3.1, the angular distribution of multipole radiation fields have an angular

distributions governed by the Legendre polynomials, with particular multipolarities having unique distributions. By measuring the angular distribution of emitted γ rays for a given de-excitation of a nucleus, it becomes possible to determine multipolarity information about a nucleus. However, in a laboratory setting, γ rays are emitted isotropically, due to the degeneracy of the magnetic substates in the initial and final states, J_i and J_f. Looking at a simple transition from $J_i = 1$ to $J_f = 0$, the allowed substates for the initial state are $m_i = $ -1,0,1, while m_f can only be 0. For the transition starting at $m_i = 0$, there is an angular distribution that varies as $\sin^2 \phi$, were ϕ is with respect to an arbitrary z-axis. The transitions for $m_i = \pm 1$ to m_f=0, the distribution varies as $\frac{1}{2}(1 + \cos^2 \phi)$ [12], with respect to the same defined axis. The total angular distribution for the emitted γ rays is then the sum of each angular distribution found for the individual substates:

$$W(\phi) \propto p_{-1}\frac{1}{2}(1 + \cos^2 \phi) + p_0 \sin^2 \phi + p_1 \frac{1}{2}(1 + \cos^2 \phi), \qquad (1.22)$$

where p_i is the population of a specific substate, such that $\sum_i p_i = 1$. If all of the states are equally populated, then $p_{-1} = p_0 = p_1 = \frac{1}{3}$ and the angular distribution is:

$$\begin{aligned} W(\phi) &= \frac{1}{3}(\frac{1}{2}(1 + \cos^2 \phi) + \sin^2 \phi + \frac{1}{2}(1 + \cos^2 \phi)) \\ &= \frac{1}{3}(1 + \cos^2 \phi + \sin^2(\phi)) = \frac{2}{3}. \end{aligned} \qquad (1.23)$$

Because the distribution is uniform, it becomes independent of direction and contains no multipolarity information.

Angular correlation measurement is a powerful experimental technique used to determine the angular distribution between two successive particles in a radioactive transition cascade. For a $\gamma - \gamma$ cascade, a nucleus rapidly emits multiple photons to reach a less energetic state. If both γ rays are emitted within a short enough time frame, then the nucleus can be assumed to remain in the same orientation for each emission. The importance of this is illustrated in a simple $0 \rightarrow 1 \rightarrow 0$ cascade, where the initial and final states are spin 0, with an intermediate state J_x being spin 1. Here, γ_1 facilitates the initial transition, $0 \rightarrow 1$, while γ_2 facilitates the final transition $1 \rightarrow 0$. The level scheme of this cascade is shown in Figure 1.1 Because the final transition is the same as the process described above, it has the same result for its distribution:

$$W(\phi) \propto p_{-1}\frac{1}{2}(1 + \cos^2 \phi) + p_0 \sin^2 \theta + p_1 \frac{1}{2}(1 + \cos^2 \phi). \qquad (1.24)$$
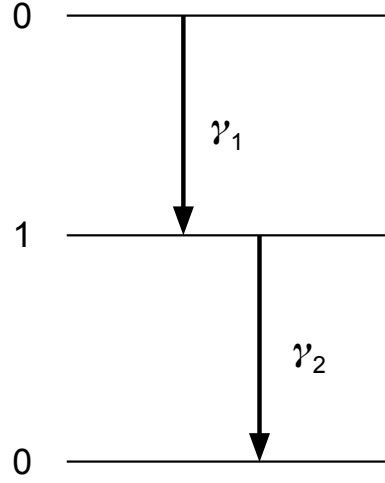
Figure 1.1: Level scheme of $0 \rightarrow 1 \rightarrow 0$ cascade.

For the first transition, $0 \rightarrow 1$, the same values for the initial and final substates exist, namely $m_x = -1, 0, 1$ and $m_i = 0$. Therefore, the distribution is identical to the second distribution, only at different angle with respect to the z-axis, θ. Hence, the total angular distribution is:

$$W(\phi, \theta) \propto p_{-1}\frac{1}{4}(1 + \cos^2\phi)(1 + \cos^2\theta) + p_0 \sin^2\phi \sin^2\theta + p_1\frac{1}{4}(1 + \cos^2\phi)(1 + \cos^2\theta).$$
$$(1.25)$$

The angular correlation method is to then define the direction of the first emitted γ ray as the z-axis. Given this orientation, the angle of the initial γ ray is forced to 0, and the angle of the second γ ray is measured with respect to the orientation of the first γ ray. Using Equation 1.25, the total angular distribution for the $0 \rightarrow 1 \rightarrow 0$ is then:

$$\begin{aligned} W(0, \theta) &\propto \frac{1}{4}(1 + \cos^2\theta)(2) + \sin^2\theta(0) + \frac{1}{4}(1 + \cos^2\theta)(2) \\ &\propto 1 + \cos^2\theta \end{aligned}$$
$$(1.26)$$

Because this method forces substates, p_i, that depend on $\sin(\phi)$ to be 0, the emitted γ rays will create an anisotropic angular distribution [14]. This result can be further
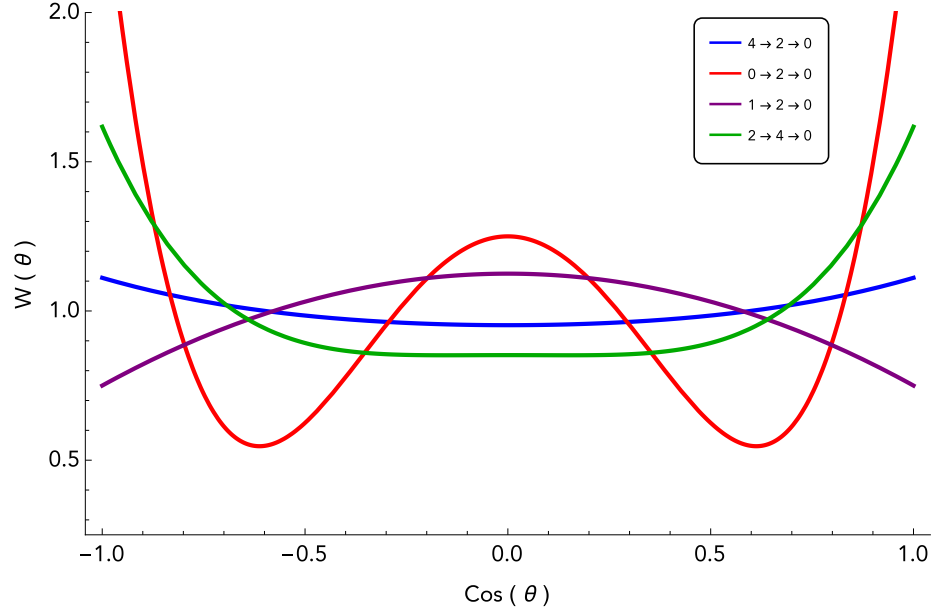
Figure 1.2: Example of angular correlations for multiple cascades.

generalized for any cascade to produce angular distributions of the form:

$$W(\theta) = \sum_{k=0,k=even}^{L} a_k P_k(\cos\theta), \tag{1.27}$$

which is also referred to as the the angular correlation function. Here, P_k are the Legendre polynomials and a_k are coefficients depending on the nuclear spins, angular momentum carried away by the transition γ ray, and the mixing ratio of the electric and magnetic multipole moments. The sum in this equation uses even iterations of k in order to conserve parity, and extends twice beyond the lowest multipolarity of the γ rays in a given cascade [12]. For a quadrupole-quadrupole cascade, the angular correlation function takes the form:

$$\begin{aligned}W(\theta) &= A_0 + A_2 P_2(\cos\theta) + A_4 P_4(\cos\theta) \\ &= A_0[1 + a_2 P_2(\cos\theta) + a_4 P_4(\cos\theta)].\end{aligned} \tag{1.28}$$

Here, a_2 and a_4 are the coefficients that depend on the physics of the system, while A_0 is a normalization factor. The angular correlations for a select number of cascades are shown in Figure 1.2.

Because the angular correlation coefficients are dependent on the spins of the initial, intermediate, and final states of a cascade, the values of these coefficients can be used to assign spin values to nuclear states. Moreover, these coefficients can be

analytically calculated using the values of physical properties for a given cascade. The coefficients a_k are described by two functions, with each dependent on one of the γ rays in a cascade:

$$a_k = A_k(\gamma_1)D_k(\gamma_2), \tag{1.29}$$

The A_k and D_k functions are given by:

$$A_k(\gamma_1) = \frac{1}{1 + \delta_1^2}[f_k(L_1, L_1, J_i, J_f) + 2\delta_1 f_k(L_1, L_1', J_i, J_f) + \delta_1^2 f_k(L_1', L_1', J_i, J_f)]$$

$$D_k(\gamma_2) = \frac{1}{1 + \delta_2^2}[f_k(L_2, L_2, J_i, J_f) + 2\delta_2 f_k(L_2, L_2', J_i, J_f) + \delta_2^2 f_k L_2', L_2', J_i, J_f)], \tag{1.30}$$

where again L' denotes the $L + 1$ multipole order present in the transition. Here, f_k are coefficients that are dependent on the multipolarities of the γ ray and the spins of the initial and final states for a single transition:

$$f_k(L_1, L_2, J_i, J_f) = (-1)^{J_f - J_i - 1}[(2L_1 + 1)(2L_2 + 1)(2J_i + 1)]^{\frac{1}{2}} \times$$
$$\langle L_1 L_2 - 1|k0\rangle W(J_i J_i L_1 L_2; iJ_f)B_k(J_i), \tag{1.31}$$

where $B_k(J_i)$ is an alignment parameter proportional to a Clebsch-Gordan coefficient and $W(J_i J_i L_1 L_2; iJ_f)$ is the Racah coefficient. For integral spin, this alignment parameter is:

$$B_k(J) = (2J + 1)^{\frac{1}{2}}(-1)^J\langle J0J0|k0\rangle, \tag{1.32}$$

and for half-integral spin:

$$B_k(J) = (2J_1)^{\frac{1}{2}}(-1)^{J - \frac{1}{2}}\langle J\frac{1}{2}J\frac{1}{2}|k0\rangle. \tag{1.33}$$

Here, the notation $\langle x|y\rangle$ denotes the calculated Clebsch-Gordan coefficients. Furthermore, the Racah coefficient is given by:

$$(-1)^{j_1 + j_2 + j_4 + j_5}W(j_1 j_2 j_5 j_4; j_3 j_6) = \begin{Bmatrix} j_1 & j_2 & j_3 \\ j_4 & j_5 & j_6 \end{Bmatrix}, \tag{1.34}$$

where the term on the right is determined by the Wigner 6j symbol:

$$
\begin{Bmatrix} j_1 & j_2 & j_3 \\ j_4 & j_5 & j_6 \end{Bmatrix} = \sum_{m_1,\ldots,m_6}^{6} (-1)^S \begin{pmatrix} j_1 & j_2 & j_3 \\ m_1 & m_2 & -m_3 \end{pmatrix} \begin{pmatrix} j_1 & j_5 & j_6 \\ -m_1 & m_5 & -m_6 \end{pmatrix}
$$
$$
\begin{pmatrix} j_4 & j_5 & j_3 \\ m_4 & -m_5 & -m_3 \end{pmatrix} \begin{pmatrix} j_4 & j_2 & j_6 \\ -m_4 & -m_2 & -m_6 \end{pmatrix}.
$$

(1.35)

Here, the Wigner 6j symbol is determined by the sum of Wigner 3j symbols and $S = \sum_{n=1}^{6}(j_n - m_n)$. The Wigner 3j are then given by Clebsch-Gordan coefficients that describe the angular momentum coupling between j_1, j_2, and j_3 and their magnetic substates:

$$
\begin{pmatrix} j_1 & j_2 & j_3 \\ m_1 & m_2 & -m_3 \end{pmatrix} = \frac{(-1)^{j_1-j_2-m_3}}{\sqrt{2j_3+1}} \langle j_1 m_1 j_2 m_2 | j_3 - m_3 \rangle.
$$

(1.36)

It should be noted here that when using these equations to calculate the angular correlation coefficients given a specific spin cascade, not all a_2 and a_4 combinations are necessarily allowed.

A more thorough derivation and explanations of the above functions required for calculating the a_k coefficients can be found in *Methods of Experimental Physics* by Williams [15], as the above functions were not personally derived. Equations 1.29 - 1.36 are later used to calculate the theoretical angular coefficients using a C++ program.

1.4 Experimental Techniques

Once an angular correlation has been measured, there exist a number of techniques to extract the spins of excited nuclear states. In S.J. Robinson's 1990 paper [3], important methods include direct correlation coefficient measurements, ellipse comparison, and goodness-of-fit vs.mixing.

The first method used to assign nuclear spins was the direct correlation of coefficient measurements, where the angular correlation coefficients a_2 and a_4 were found directly by performing a quadratic fit in $\cos^2(\theta)$ to the experimental data. This technique required corrections for the opening angle of the detectors and attenuation due to the interaction of any long-lived intermediate states with extranuclear fields. Although this method was initially popular for its relatively easy implementation, as Robinson describes, it uses a linear least squared fit, which can lead to a misinterpre-
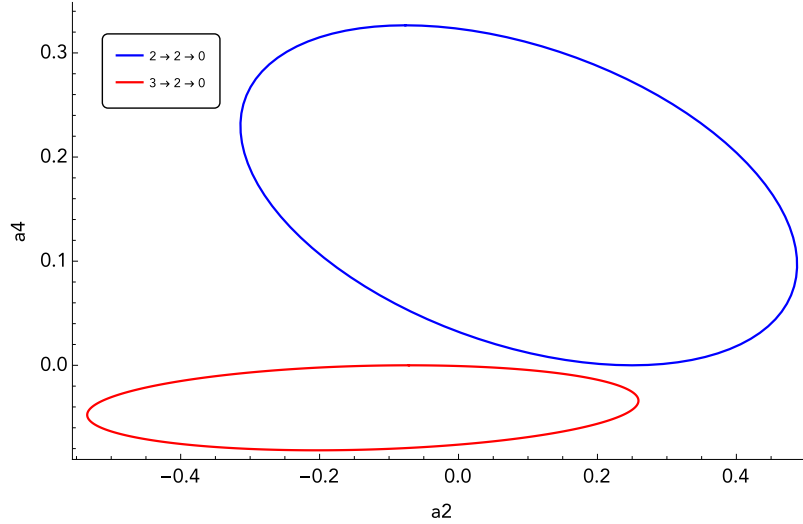
Figure 1.3: Physical angular correlation coefficients for the $2^+ \rightarrow 2^+ \rightarrow 0^+$ and $3^+ \rightarrow 2^+ \rightarrow 0^+$ cascades for varying δ.

tation of the data where perfectly acceptable conclusions are rejected [3].

For angular correlations involving a single mixing ratio, it is convenient to use ellipse comparisons. With this method, the different values of a_2 and a_4 are plotted against each other in order to visualize potential overlap in values. For a measured pair of coefficients, if the error between the coefficients only overlaps a single ellipse using a certain level of confidence, then it is with a good assumption that the measured coefficients belong to that cascade. If the error overlaps multiple ellipses, then no distinction can be made between nuclear spins, as the coefficients do not discriminate between different cascades. An example of this can be seen in Figure 1.3, where the values of the angular coefficients for the $2^+ \rightarrow 2^+ \rightarrow 0^+$ and $3^+ \rightarrow 2^+ \rightarrow 0^+$ cascades are in close agreement for $a_2 \approx 0.1$ or $a_4 \approx 0.05$

The preferred method suggested by Robinson was the goodness-of-fit vs. mixing ratio. This technique uses a non-linear least squares fit to the angular correlation function, $W(\theta)$, using a single mixing ratio as the fitting parameter. By extracting the reduced chi-square (χ^2/ν) between the experimental and and theoretical $W(\theta)$ values, the resulting plot of χ^2/ν against $\arctan(\delta)$ can be used to find minima. For the minima that fall under a certain confidence limit, the spins associated with the $W(\theta)$ of that cascade can be assigned. The example Robinson used in his paper can be seen in Figure 1.4, where the χ^2/ν is plotted against $\arctan(\delta)$ for three different cascades at two confidents levels. Here, because each cascade falls below the 2σ limit, the corresponding spins statistically agrees with the data, and no definitive value for spin can be assigned.
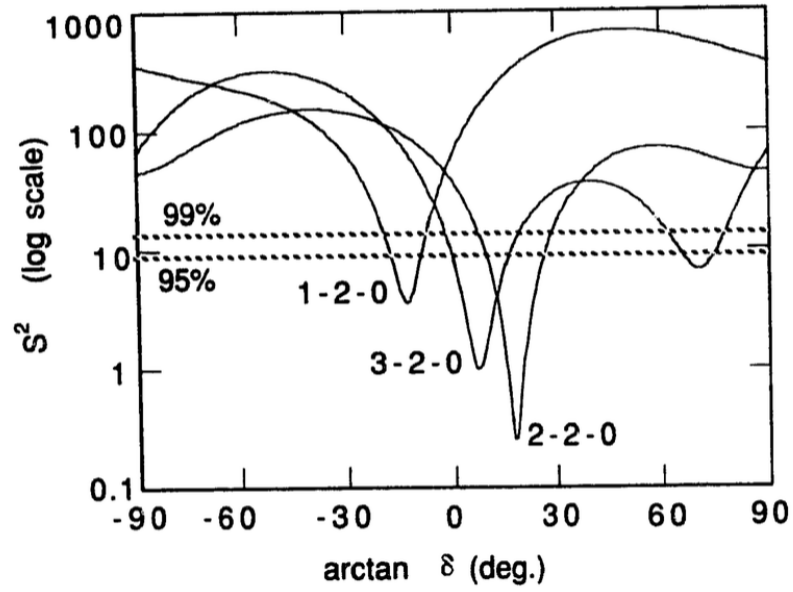
Figure 1.4: Reduced chi-square against $\arctan(\delta)$ for an experimentally measured cascade of ^{146}Nd and three theoretical correlations with a varied mixing ratio. [3]

Although the goodness-of-fit test was shown by Robinson to be the most effective in distinguishing between nuclear spins, the method he used to find the reduced chi-square involved using the values calculated from the theoretical angular correlation function. As is shown in the following chapters, the theoretical angular coefficients do not necessarily provide the best fit to experimental data, due to the finite resolution and complex geometry of the GRIFFIN spectrometer. Instead, the goodness-of-fit test was performed by using Monte Carlo simulations in place of the theoretical angular correlations, in order to achieve more accurate results.

Chapter 2

Experiment and Simulation

This chapter discusses the means to produce an angular correlation, both experimentally and through simulation. The physical interactions that make γ-ray detection possible are described before going into an explanation of the characteristics of the GRIFFIN spectrometer. The methods behind simulating γ-ray detection with GRIFFIN and extracting an angular correlation with simulated data are discussed in the final section.

2.1 γ Ray Interactions with Matter

Detectors built for γ-ray spectroscopy fall into two categories: scintillators, such as sodium-iodide (NaI) or semi-conductors, such as high-purity germanium (HPGe) crystals. Scintillation detectors use crystals that emit light when γ rays interact with the atoms in the crystals, where the intensity of the light produced is proportional to the energy deposited in the crystal by the γ ray. Semiconductor detectors are fundamentally different from scintillation detectors in that they rely on the direct detection of charge carriers generated by photons. In a HPGe detector, a voltage is applied across the crystal volume of germanium, a semi-conductive material. When an incident photon with enough energy moves an electron from the valence band into the conduction band, the electron moves to the positive contact, and the negative hole moves to the negative contact. The arrival of both charges at the contacts provides a clean signal, and produces a significantly higher energy resolution than a NaI detector [16].For both methods to work, light must interact with matter in order to produce a signal. The effects in energy resolution between the two type of detectors can be seen in Figure 2.1, where the variance in energy for the NaI detector is wider with

two degrees less γ rays recorded.
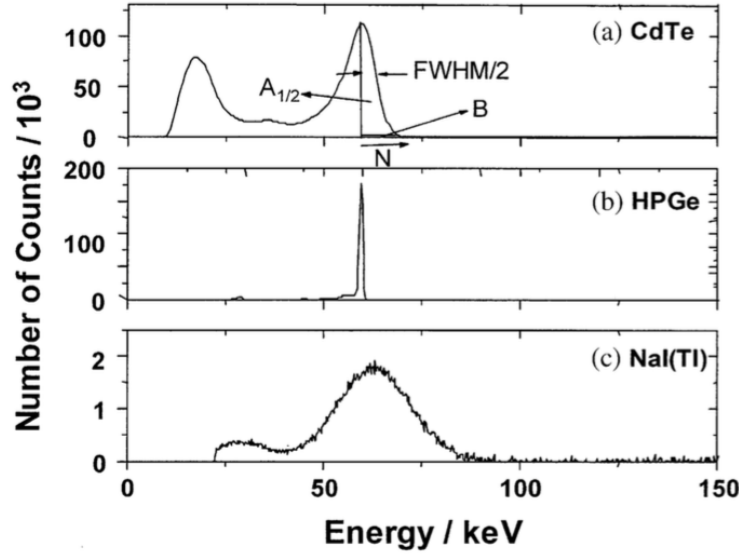
Figure 2.1: A comparison of CdTe, HPGe and NaI detectors used for γ-ray spectroscopy with γ rays from a ^{241}Am source [4].

The most common physical interactions associated with γ rays and detector material are photoelectric absorption, Compton scattering, and pair production. The probability per unit length of γ-ray interaction with matter is given by the total linear attenuation coefficient μ:

$$\mu = \tau + \sigma + \kappa, \tag{2.1}$$

where τ, σ, and κ are the individual linear attenuation coefficients for photoelectric absorption, Compton scattering, and pair production, respectively, given in units of reciprocal length. In Figure 2.2, the total linear attenuation coefficient is plotted as a combination of the three individual coefficients for an HPGe detector. These processes are essential for understanding γ-ray detection and the backgrounds encountered.

2.1.1   Photoelectric Absorption

Of the three processes outlined in this section, photoelectric absorption is the dominant interaction process for low-energy photons (Figure 2.2). This process is the interaction of a photon with an atom, where a complete transfer of energy occurs. As a photon is absorbed by an atom, a photoelectron is produced and ejected from the
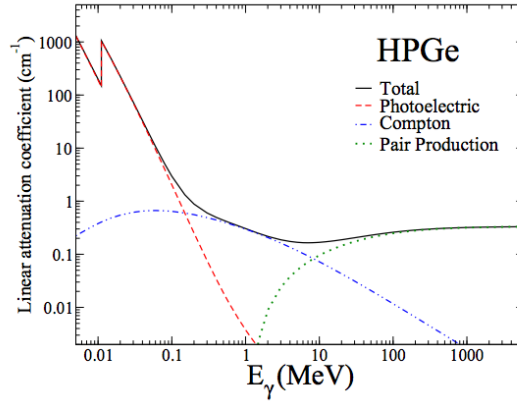
Figure 2.2: Plot of the linear attenuation coefficients for photoelectric abrobsion, Compton scattering, and pair production for HPGe and bismuth germinate (BGO) [5].

atom. The energy of the photon transferred to the electron is given by:

$$E_{e^-} = E_\gamma - E_b \tag{2.2}$$

where E_b is the binding energy of the electron to a given nucleus. The hole created by the electron is filled by either the capture of a free electron from a nearby atom or the de-excitation of an electron from another shell. In turn, this will emit characteristic X-rays or Auger electrons that can be measured by a detector [17].

The likelihood of photoelectric absorption is high for low γ-ray energies, as well for atoms containing a high atomic number, Z. The probability of this process is approximated by:

$$\tau \propto \frac{Z^n}{E_\gamma{}^{3.5}}, \tag{2.3}$$

where n is roughly between 4 and 5 for a given E_γ [18]. The strong dependence on Z in the above probability is the reason why high Z materials, such as lead or tungsten, are used for γ-ray shielding.

2.1.2   Compton Scattering

Compton scattering occurs when an incident photon scatters off an electron at an angle θ from its original direction, rather than being absorbed by the atom. In this interaction, a portion of energy in the γ ray is transferred to the electron, which then recoils at a scattering angle ϕ (See Figure 2.3).
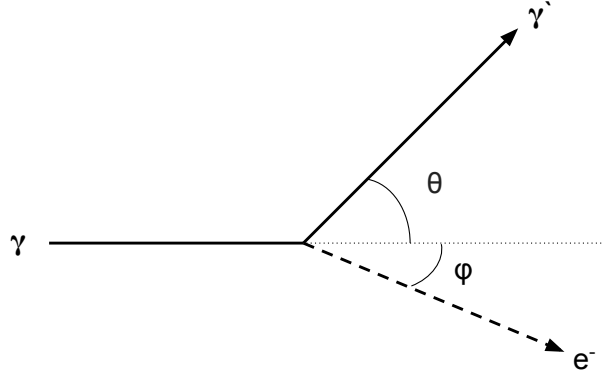
Figure 2.3: Schematic of Compton scattering

Because the incident photon loses momentum in this process, the change in wavelength of the γ ray is given by:

$$\Delta\lambda = \frac{h}{m_{e^-}c}(1 - \cos\theta) \tag{2.4}$$

[19]. In terms of energy, the above can be rewritten as:

$$E'_\gamma = E_\gamma \left[1 + \frac{E_\gamma}{m_{e^-}c^2}(1 - \cos\theta)\right]^{-1}, \tag{2.5}$$

with E'_γ being the change in the incident γ-ray energy. Here, E'_γ is equal to the energy deposited in the recoil electron, which is also equal to the energy measured by the detector. This process is typically the dominant interaction for typical γ-ray energies experienced in low-energy nuclear experiments ($0.1 < E < 10\text{Mev}$ for HPGe), as shown in Figure 2.2 [20].

Depending on the initial energy of the γ ray, Compton scattering events can occur multiple times until enough energy is lost for the photon to be photoelectrically absorbed. If the photon exits the absorbing material after going through one or more Compton scattering events, only a fraction of the incident photon energy is left in the detector. When this process occurs, it gives rise to the Compton-continuum, a background effect below the full energy photopeak of the emitted γ ray (Figure 2.4). If the incident photon collides with an electron and backscatters (with $\theta \approx 180°$), then the maximum amount of energy possible is transferred to the electron and produces the Compton edge [17].

The probability of Compton scattering is directly proportional to the number of electrons in the detector material, as well as the atomic number of the material:
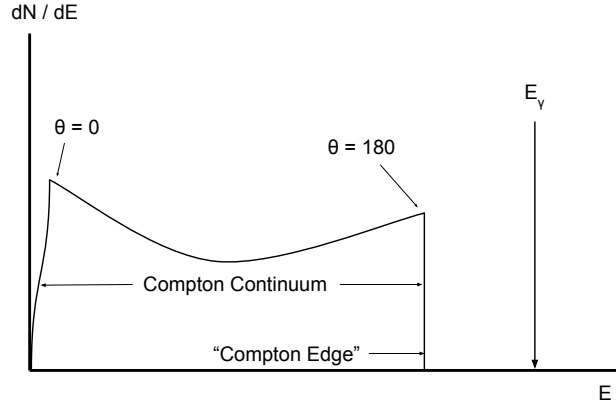
Figure 2.4: Schematic of Compton scattering background effects

$$\sigma = \sigma_c Z N, \tag{2.6}$$

where σ_c is the cross section of an electron and N is the number density of electrons. To mitigate the Compton background, suppressors are made from dense, high-Z materials such as BGO to maximize the probability of Compton scattering and photoelectric absorption.

2.1.3 Pair Production

Every particle is known to have an associated antiparticle, with every particle-antiparticle annihilation producing two γ rays. Similarly, a γ ray with an energy above twice the rest mass of an electron (or 1.022 MeV) can interact with the Coulomb field of a nucleus in the detector material, producing a electron-positron pair. This process is known as pair production, and is the dominant γ-ray interaction for energies above 5 MeV [21].

The energy of the electron-positron pair is split between the energy of the incident photon:

$$E_e^- + E_e^+ = h\nu - 2m_0 c^2. \tag{2.7}$$

As the positron travels through the detector material, it gives up energy via collisions or bremsstrahlung[1] and comes to rest before annihilating with an electron. This annihilation then produces two γ rays at 0.511 MeV each. If either one or both of

---
[1]See Section 2.1.4

these γ rays escapes the detector material, then the measured energy of the initial γ ray will be 0.511 or 1.022 MeV less than its actual value. This process manifests itself as single- and double-escape peaks, respectively. Although fairly easy to recognize in a simple γ-ray spectrum, escape peaks can become an issue if peaks of interest are in those energy ranges.

The probability of pair production, given by the linear attenuation coefficient κ, is proportional to $\sqrt{Z}$ and is significant for high-Z materials [22].

2.1.4   Secondary Radiation

Secondary radiation occurs when γ rays that are not produced from the decay of a particular nucleus interact with the detector material. For example, when characteristic X-rays are produced during photoelectric absorption they can leave the detector they were created in and interact with another detector. Additionally, when a photoelectron is ejected, it can undergo accelerations caused by the surrounding atoms. When this occurs, braking radiation from the accelerated electron, called bremsstrahlung, can interact with the detector if escape occurs. Furthermore, bremsstrahlung can occur if unwanted β particles are emitted from the nucleus and interact with the detector.

If the effects of surrounding materials is taken into effect, such as an enclosure structure surrounding a detector used for background radiation prevention, then it becomes possible for the primary radiation to react with the material to cause secondary radiation to interact with the detector. The most common of these reactions involve what is called backscatter, escape radiation reflected back onto the detector via Compton scattering. Peaks from this usually occur around 0.2-0.25 MeV on the response function, due to maximum energy a photon produced from Compton
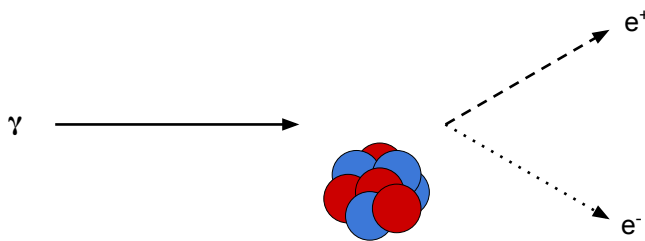
Figure 2.5: Schematic of pair production

scattering can have:

$$h'\nu|_{\theta=\pi} = \frac{h\nu}{1 + 2h\nu/m_{e^-}c^2} \approx \frac{m_{e^-}c^2}{2}, \tag{2.8}$$

taking the high-energy limit of the initial photon ($h\nu \gg m_{e^-}c^2$) [17]. In addition, characteristic X-rays and annihilation radiations can also be produced by primary radiation from the detector. To combat this effect, high-Z materials - those most effective at protecting the detector from background noise- are lined with low-Z material in order to reduce the probability of secondary radiation occurring.

The magnitude of the effects of escape and secondary radiation is correlated to the size and shape of the detector. For small detectors, where the size of detector is small relative to the mean free path of secondary radiation ($<$ 1-2 cm), most of the secondary radiation will escape interaction with the detector. For larger detectors, all secondary photons interact with the detector, resulting in a single signal, full energy γ ray peak. This single signal is due to the summing effects of the various responses. Most detectors are of intermediate size, and therefore include properties of large and small detectors, along with the potential of partial recovery of secondary radiation. Here, the possibility of backscatter is most likely. Additionally, in the event of pair production, intermediately sized detectors can allow for the escape of one of the two annihilation photons, while recording the energy of the one absorbed. Here, there is only a single escape peak with an energy of 511 keV less than the original γ-ray energy. Given the effects of detector size on γ-ray detection, the geometry of the detector becomes important. In order to make accurate assumptions about the experimental process and predict reliable outcomes, simulation is often needed due to the large number of different parameters within the system.

2.2   The GRIFFIN HPGe Detector

The Gamma Ray Infrastructure For Fundamental Investigations of Nuclei (GRIF-FIN) is a state-of-the-art HPGe high efficiency γ ray spectrometer located at the TRIUMF-ISAC-I facility in Vancouver, Canada. GRIFFIN uses 16 large clover-type detectors, each with four high-purity germanium crystals, providing excellent γ ray energy resolution [23].

The geometry of GRIFFIN is set up in a rhombicuboctahedron configuration, with 16 of the 18 square faces holding clover detectors and the 2 remaining remaining open for the beam path. In order to achieve this configuration, each HPGe crystal is cut

<div align="center">(a)   (b)</div>
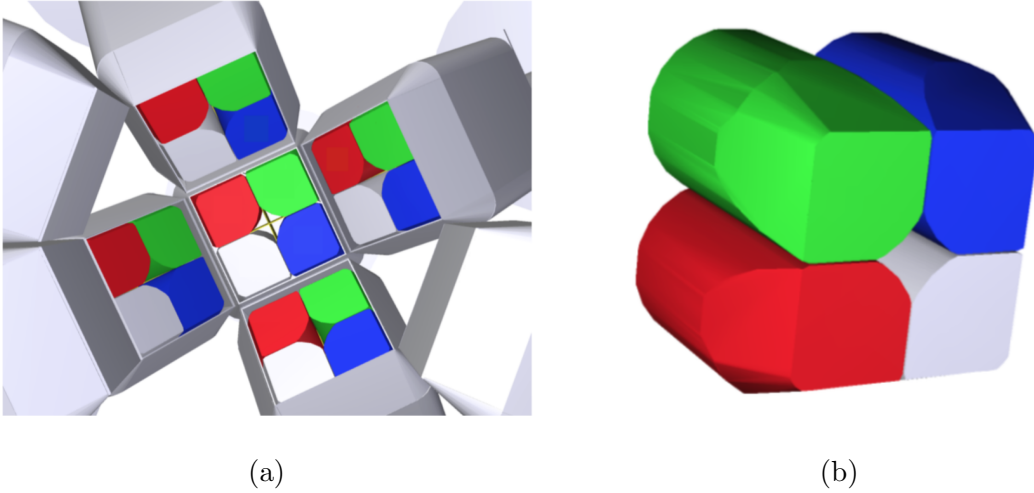
Figure 2.6: Geant4 simulated images of (a) GRIFFIN clover detectors in the experimental configuration and (b) a single GRIFFIN detector showing four HPGe crystals with tapered geometry[6].

to an initial size of 90 x 60 mm, and then given tapered edges as shown in Figure 2.6. This design gives an optimal solid angle coverage, allowing for efficient angular correlation measurements [23]. The entire GRIFFIN array can also be reconfigured into a high-efficiency mode, with the detector faces at 11 cm from the array center, or maximum peak-to-total ratio mode, with the faces at 14.5 cm from the center.

The experimental process for γ-ray spectroscopy using the GRIFFIN detector begins with the Isotope Separator and Accelerator (ISAC) facility, which produces high-quality beams of radioactive ions at low energy. This process is accomplished using the Isotope Separation On-Line (ISOL) technique, which consists of primary beam production, a target/ion source, a mass separator and a secondary beam transport system [24]. Once the Rare Isotope Beam (RIB) is produced, it is delivered to the GRIFFIN detector at ~ 30 keV, where it is deposited on an aluminum mylar tape located at the center of the GRIFFIN array. The tape is used to stop the beam and remove the daughter nucleus once the decay is completed. [23].

After the beam is deposited on the tape, the particular isotope produced is free to decay. In order for the germanium detectors to detect the emitted γ rays at a high-energy resolution, each crystal is held at a temperature below $-175°$C and is applied with 3500 V of reverse biasing voltage [25]. At FWHM, the energy resolution of GRIFFIN is around 1.9 keV for 1.33 MeV γ rays [26]. GRIFFIN has a timing resolution of 10 ns for γ-ray energies above 100 keV [27].
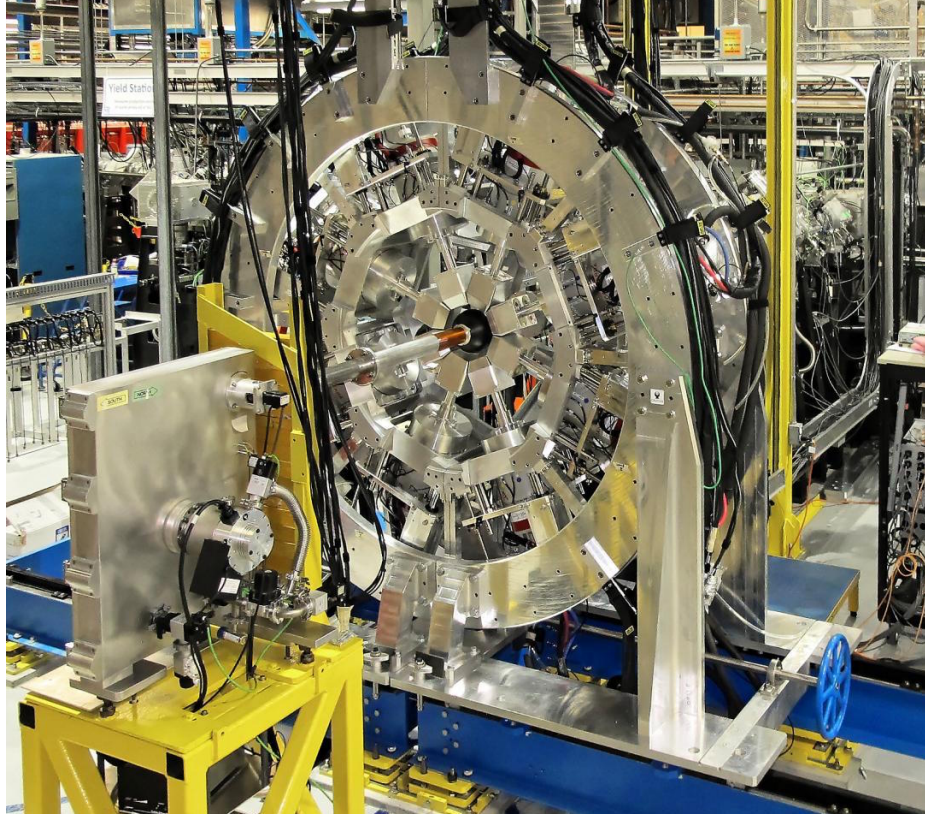
Figure 2.7: GRIFFIN detector with four clover detectors removed and beam path on the right.

2.2.1 Angular Properties

With the 64 individual HPGe crystals that make up the GRIFFIN array, there are 4096 crystal pairs, as well a crystal paired with itself when two γ rays in a given cascade interact and deposit their energy in the same crystal. These 4096 crystal pairs create 52 distinct opening angles that range from 0 to 180°. When a particular nucleus decays via a cascade of γ rays, the angle between a pair of coincident γ rays can be measured by knowing which detector each γ ray hit and then utilizing a map of opening angles. To produce the map of angles between crystal pairs, two vectors are assigned to crystal centers:

$$\mathbf{v}_i = (r \sin \theta_i \cos \phi_i, r \sin \theta_i \sin \phi_i, r \cos \theta_i) \tag{2.9}$$

$$\mathbf{x}_n = (\delta_j c_p, \delta_k c_p, d_i) \tag{2.10}$$

where $i = 1, 2$ for the two detectors and $j = 1, 2, 3, 4$ for each crystal in a detector. The distance from the center of the array to a detector face is given by r, and the

distance from the center of the detector to the center of a crystal is given by c_p. d_i is the average interaction depth of the γ ray and $\delta_{j,k}$ is either ± 1, depending on which crystal $\mathbf{x}_n$ is pointing to. As $\mathbf{x}_n$ is rotated with respect to θ and ϕ for all possible combinations of crystals, the two vectors are added together and the dot product is taken for each detector pair, producing the opening angle:

$$\theta = \cos^{-1}\left[\frac{(\mathbf{x}_{n,1} + \mathbf{v}_1) \cdot (\mathbf{x}_{n,2} + \mathbf{v}_2)}{\left\|(\mathbf{x}_{n,1} + \mathbf{v}_1) \cdot (\mathbf{x}_{n,2} + \mathbf{v}_2)\right\|}\right] \tag{2.11}$$

Each opening angle and its associated weight, or the number of occurrences, is accounted for in Table 2.1.

Given the geometry of each HPGe crystal, with each being roughly 60 x 90 mm, the γ ray interaction point inside the crystal will correspond to a different angle. Restated, as the interaction depth of a γ-ray in a crystal changes, the angle will change as a function of γ ray energy because the interaction point in a detector is a function of γ ray energy. In order to account for this phenomena, opening angles were calculated over a range of γ-ray energies to produce a mapping of the effective average opening angle as a function of energy [6]. The result of this mapping was incorporated into the γ decay simulations used in this thesis, which is further discussed in the following section.

2.3   Simulation

The method for producing radioactive decay simulations for the GRIFFIN geometry is outlined here. Angular correlation simulations were created through the Geant4 framework, using version 10.01.p03 with several modifications [28] [29]. Data analysis was performed using GRSISort - an extension of the ROOT data analysis framework edited for specific use by the GRIFFIN collaboration group. The source code for the GRIFFIN specific software packages can be found on the collaboration's Github page– `https://github.com/GRIFFINCollaboration`. Additionally, an installation guide for the software used in this thesis is described on my personal Github page–`https://github.com/wilashfie`.

2.3.1   Geant4 and Supplementary Packages

Geant4 is a C++ toolkit used to simulate the interactions of particles passing through matter. The code, which stands for *GEometry ANd Tracking*, was originally devel-

Ang. Index	Open Angle (°)	Weight	Ang. Index	Open Angle (°)	Weight
1	0.00	64	27	91.52	128
2	18.78	128	28	93.76	48
3	25.60	64	29	93.77	64
4	26.69	64	30	96.95	64
5	31.94	64	31	101.33	64
6	33.65	48	32	103.61	96
7	44.36	128	33	106.91	64
8	46.79	96	34	109.14	96
9	48.57	128	35	110.13	64
10	49.79	96	36	112.54	64
11	53.83	48	37	113.35	64
12	60.15	96	38	114.98	96
13	62.70	48	39	116.91	64
14	63.08	64	40	117.29	48
15	65.01	96	41	119.84	96
16	66.46	64	42	126.16	48
17	67.45	64	43	130.20	96
18	69.86	64	44	131.42	128
19	70.86	96	45	133.20	96
20	73.08	64	46	135.63	128
21	76.38	96	47	146.34	48
22	78.66	64	48	148.05	64
23	83.04	64	49	152.31	64
24	86.22	64	50	154.39	64
25	84.23	48	51	160.21	128
26	88.47	128	52	180.00	64

Table 2.1: The 52 distinct opening angles - given in angular index and degrees - between each crystal in the GRIFFIN geometry and the corresponding weights (number of shared angle pairings).

oped by CERN for simulating the geometry and physical processes seen in high-energy physics experiments. The simulations are built around user defined geometries that account for volume, material, and location in space - usually modeled after a specific particle detector. After the geometry is designed, simulations are run by firing particles (γ rays, β particles, etc.) in a set direction. As the particles travel through different volumes, their location of interaction and the energy deposited in a material is determined by Monte Carlo methods, and is recorded for the duration of the simulation [28].

The two simulation classes under the the Geant4 framework specifically modified

for the GRIFFIN spectrometer were the Radioactive Decay and Photon Evaporation modules. The first is used to simulate the decay of radioactive nuclei by α, β^+, and β^- emission, as well as electron capture. If the daughter of a given nuclear decay is in an excited state, then its nuclear de-excitation is simulated using the Photon Evaporation class. Within the modules used are predefined decay files of roughly 3000 nuclides, which contain information on level structure, branching ratios, γ-ray energies, and other empirically derived data from the Evaluated Nuclear Structure Data Files (ENSDF) [30].

In addition to the two Geant4 classes, the Gamma-Gamma Angular Correlations (GGAC) code was installed as a small extension to the existing radioactive decay class. The package allows for two additional user defined inputs to the radioactive decay simulation that override the normal isotropic emission of γ rays and produce an anisotropic angular distribution. These inputs consist of files that contain γ-ray multipolarity information, mixing ratios of the emitted γ rays, and the ground state angular momentum of the daughter nucleus.

In order to run radioactive decay simulations as they would occur for an experiment using the GRIFFIN detector, a simulation package was written by the GRIFFIN Collaboration group replicate the GRIFFIN array geometry in a Geant4 environment.

2.3.2   Creating Simulated Angular Correlations for ^{60}Co

With the GGAC and GRIFFIN simulation extensions installed, the angular distributions of emitted γ rays will become anisotropic. To build a γ-ray angular correlation, an excited state must first be chosen, where it is populated to emit successive γ rays without passing through a long-lived state (See Section 1.3). The source chosen for this thesis was Cobalt-60, as it has been studied extensively and is known to β^- decay to the 2.5 MeV, 4^+ state of ^{60}Ni with a branching ratio of nearly 100%. Once in the excited state of ^{60}Ni, the nucleus then emits a cascade of γ rays at 1173 and 1332 keV that is then used to make angular correlation measurements. The level scheme for this decay is shown in Figure 2.8, while the γ-ray spectrum with the two photopeaks is shown in Figure 2.9.

With ^{60}Co chosen as the source nucleus, simulations were run for a number of $\gamma-\gamma$ decay events after two values of spin (J_i), four multipolarities (L_i), and two mixing ratios (δ_i) were assigned given a specific cascade. After a simulation was complete, a $\gamma-\gamma$ coincidence matrix was created. The matrix created here is a 3D histogram, containing the spectrums of the detected γ rays on the x and y axes, and a count
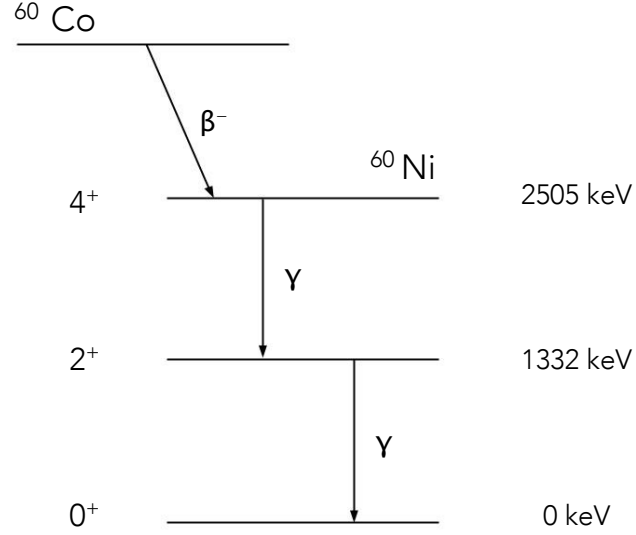
Figure 2.8: Decay of ^{60}Co to ^{60}Ni.
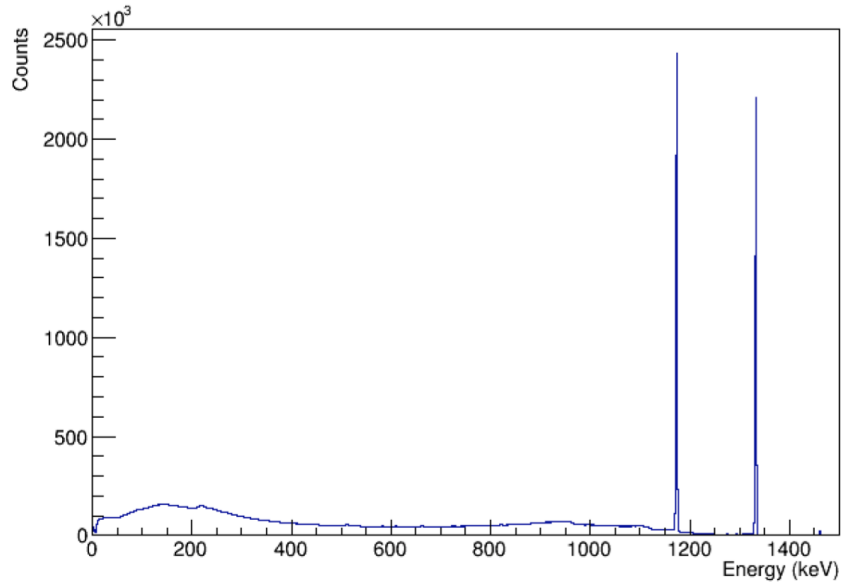
Figure 2.9: γ-ray spectrum of ^{60}Co decay.

of the opening angles between the detector crystals hit by two coincident γ rays on the z-axis. Here, the count of the distinct angles is referred to as the angular index, where each opening angle is indexed from 1 to 52. Figure 2.10 shows a 2D version of the $\gamma - \gamma$ coincidence matrix without the projection of the z-axis. Here, the color represents the count of the number of coincedences recorded.

The information needed for an angular correlation is found in the two photopeak energies of the $\gamma - \gamma$ matrix. In order to isolate the energies, the three dimensional
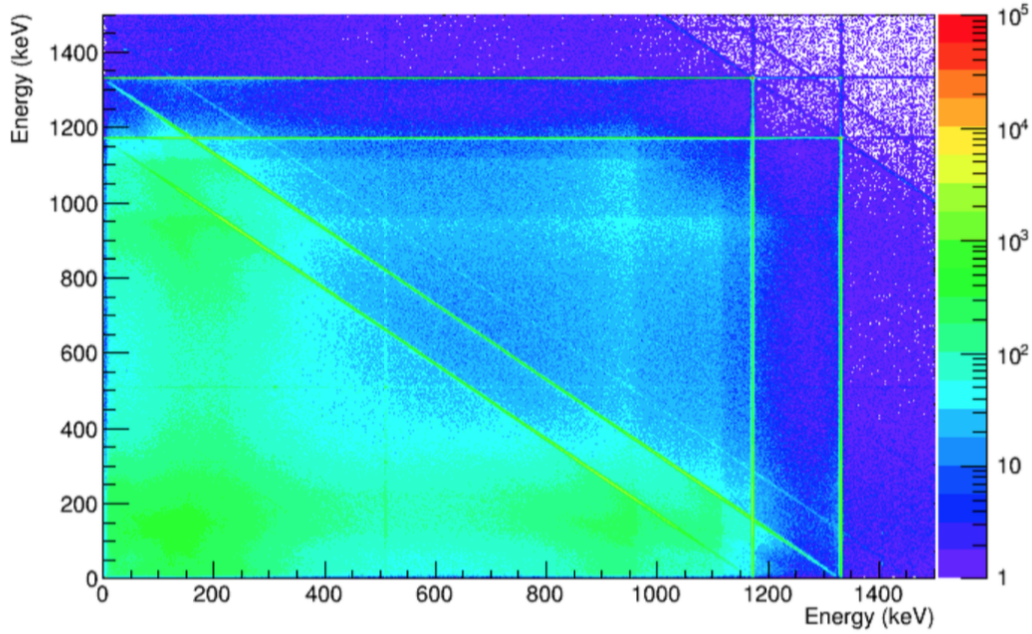
Figure 2.10: γ-γ coincidence matrix with γ ray energy recorded on the x and y axis. Color represents the frequency of coincidence for the recorded cascade.

histogram was first gated on the higher γ ray energy, 1332 keV, creating a two dimensional histogram of angular index and energy. This histogram was then gated on the lower γ ray energy, 1173 keV, which creates a one dimensional histogram of coincidence counts for each angle is created for the $\gamma - \gamma$ decay of ^{60}Co, as shown in Figure 2.11. However, the spectrum here is heavily skewed by the 4096 detector pairs that contribute to the angular indexes. By dividing out the associated weights of the opening angles, a normalized angular correlation is created in terms of angular index (Figure 2.12). Finally, angular index was converted to angles to more accurately represent the angular correlation in terms of $\cos(\theta)$ (Figure 2.13).

The process of creating an angular correlation from simulated data was performed with help from the TAngularCorrelation class in GRSISort [32]. Furthermore, in addition to the effect of crystal penetration depth created by varying the γ-ray energies, detector efficiency is also affected. High energy γ rays are more likely to produce scattering between detectors, and thus a less likelihood of full energy deposition in a single crystal. As this process is controllable in a Geant4 environment, all simulations performed in this thesis were done in single crystal mode. More information on how to perform the simulation process is provided in Appendix A.
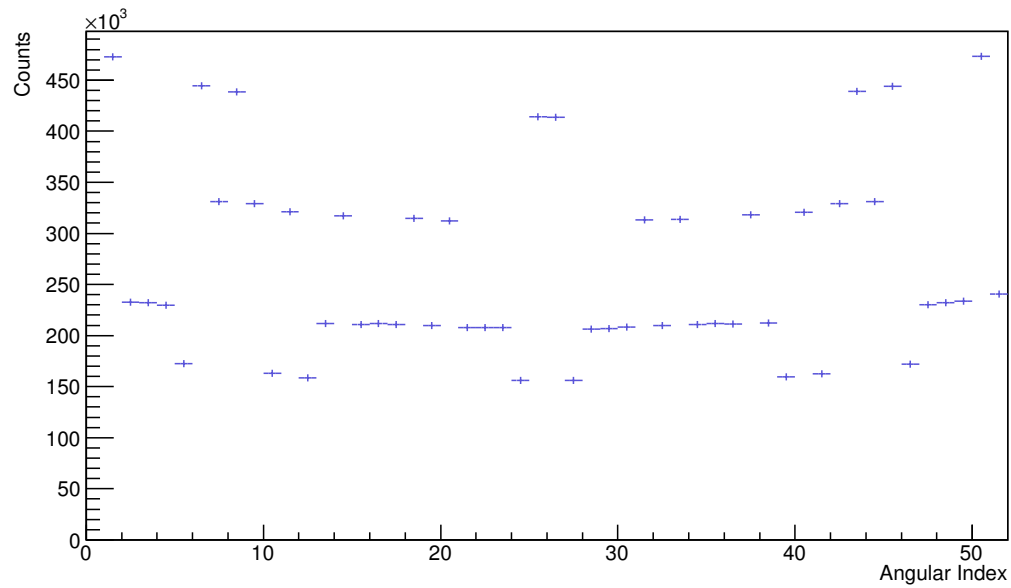
Figure 2.11: Un-normalized angular index histogram for a simulated $4^+ \rightarrow 2^+ \rightarrow 0^+$ cascade at 10^9 events. Symmetric effects are due to the weighted distributions of angle openings of the GRIFFIN spectrometer.
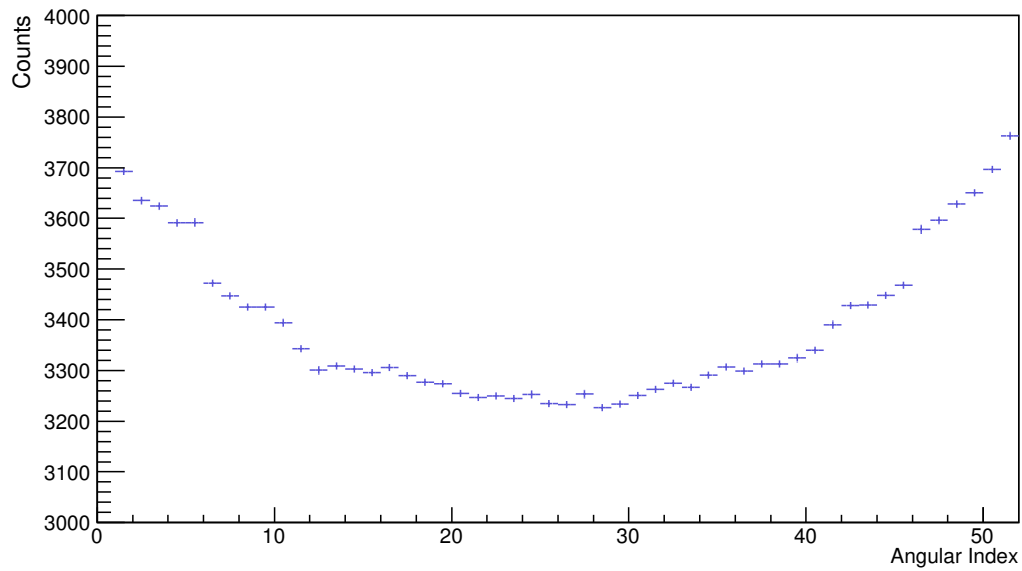
Figure 2.12: Normalized angular index histogram for a simulated $4^+ \rightarrow 2^+ \rightarrow 0^+$ cascade at 10^9 events.
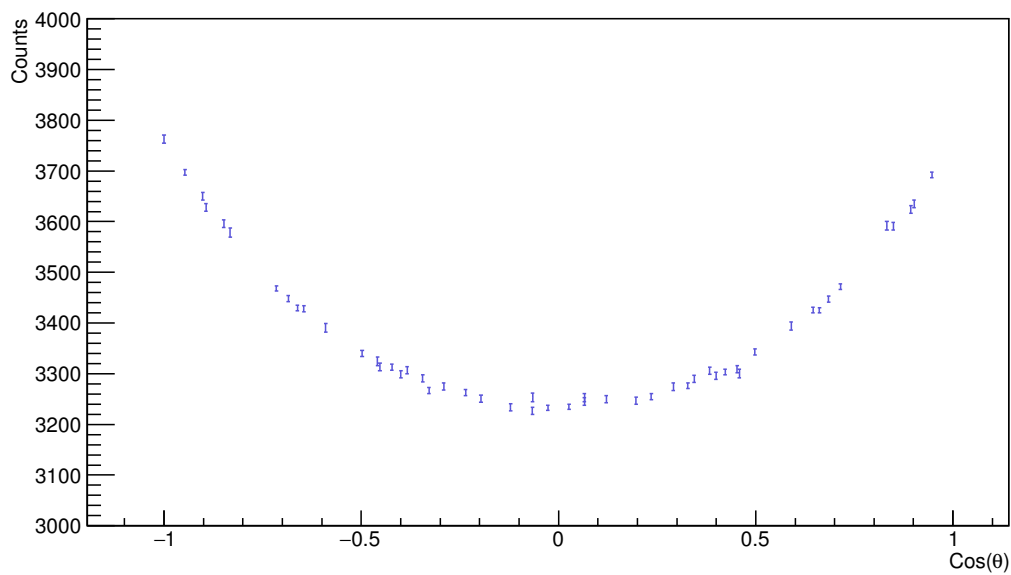
Figure 2.13: Simulated angular correlation for a $4^+ \to 2^+ \to 0^+$ at 10^9 events. Here, the normalized number of coincidences is plotted against $\cos(\theta)$.

Chapter 3

Reduced Simulations

3.1   Background

Once an angular correlation histogram is created from data, the objective becomes to extract the angular coefficients a_2 and a_4 that describe the angular distribution $W(\theta)$:

$$W(\theta) = A_0[1 + a_2 P_2(\cos\theta) + a_4 P_4(\cos\theta)]. \tag{3.1}$$

Using GRSISort, the process of fitting data is easily accomplished by defining and fitting the $W(\theta)$ distribution to the experimental angular correlation data using a non-linear least squares method. Figure 3.1 shows a fit to a $0^+ \rightarrow 2^+ \rightarrow 0^+$ cascade, where the solid red line is the fit to the data and the dashed blue line is the $W(\theta)$ distribution using the physical a_2 and a_4 coefficients. Here, it becomes important to notice the discrepancy between the distribution produced from the fit and the expected distribution produced from the theoretical coefficients. Because each GRIFFIN detector has finite angular and energy resolutions, a complex geometry, and irregularities due to γ-ray interactions with matter, the angular distribution of γ rays become distorted by these properties. The result of the effects of the detector are reflected in the measured values of a_2 and a_4, which vary to a small degree from

Coefficient	Physical	Fitted
a_2	0.3571428	0.27 ± 0.008
a_4	1.1428571	0.92 ± 0.01

Table 3.1: Theoretical and measured coefficients for a $0^+ \rightarrow 2^+ \rightarrow 0^+$ cascade at $\delta = 0$.
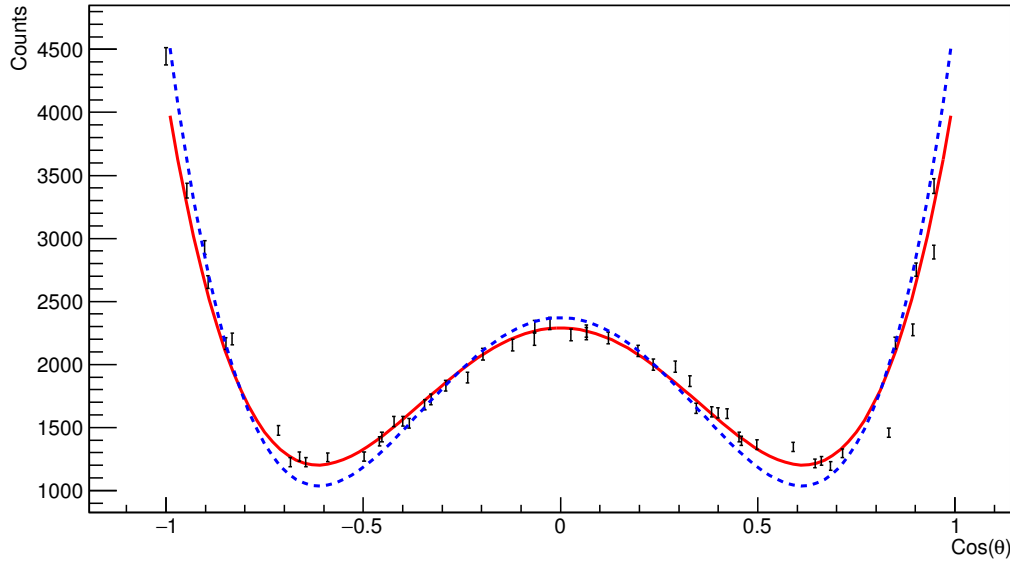
Figure 3.1: Angular correlation for the $0^+ \to 2^+ \to 0^+$ cascade with fit (in red) and theoretical (in blue) $W(\theta)$ distributions.

their theoretical values. For clarification purposes, the measured values of a_2 and a_4 that contain the distorting effects of the GRIFFIN detectors will be denoted as c_2 and c_4 for the remainder of this thesis. Given the fit to experimental data shown in Figure 3.1, the comparison between the fitted and physical coefficients are explicitly shown in Table 3.1.

By simulating angular correlations produced in a $\gamma - \gamma$ cascade, it becomes possible to make more accurate comparisons between theory and experimental data. This comparison is done in part to identify bias in an instrumental response to real experimental conditions, or to identify contradictions to nuclear theory that could ultimately lead to discovery. In most cases, as is the case here, the purpose of simulated and experimental angular correlation data is to correctly determine and assign the spins of nuclear states in a given cascade, and the multipolarities and mixing ratios in a $\gamma - \gamma$ transition.

As was discussed earlier[1], the most effective method to assign spin states is to use a goodness-of-fit test between the experimental data and theoretical angular correlation functions. In the past, this method was easily accomplished due to the simple design of early detectors. The detectors, usually cylindrical in shape, were moved to different locations to get intensities at a number of angles, which when combined

------

[1] See Section 1.4

with a geometric correction factor, Q, determined the angular correlation coefficients [31]. The Q value here, found by integrating over the solid angle of a detector face, was an easy analytic calculation due the simple geometries of the detectors. With GRIFFIN, the use of 16 clover detectors in a rhombicuboctahedron configuration, each containing four HPGe crystals with tapered edges, makes the Q-values needed for solid angle correction much more difficult to determine analytically. In addition, with the detectors in close proximity the Q value can be further affected by Compton scattering effects. Instead, the goodness-of-fit test is accomplished with simulation taking the place of the theoretical angular correlation function.

The method used to perform the goodness-of-fit test for spin assignments at GRIF-FIN was developed by Andrew MacLean [6]. He created a library of templates: a set of high statistic Geant4 angular correlation simulations for different nuclear spin values, mixing ratios, and γ-ray energies made for the specific purpose of comparison between simulated and experimental data. By comparing the templates to experiment, the problems associated with fitting experimental data to theoretical angular correlations are alleviated as the templates inherently contain the distorting effects that arise from the properties of the detector.

The process of performing a goodness-of-fit test begins with creating a single template for an angular correlation, where the spins, angular momenta, and mixing ratios of the specific cascade are chosen for the specific cascade to be compared to experimental data. From here, the information about the chosen cascade is used to calculate the theoretical a_2 and a_4 coefficients. The unique angular distribution these coefficients describe, $W(\theta)$, is simulated appropriately using the Geant4 framework under detector specific properties; creating a simulated angular correlation (e.g. template). The template is then compared to experimental data using the χ^2 statistic:

$$\chi^2 = \sum_i^n \frac{(O_i - E_i)^2}{\sigma_i^2}, \tag{3.2}$$

where E_i is the low-statistics experimental data and O_i is the high-statistics simulation. The combined error is given by σ_i. Because the high-statistics error is much less than the error found in the low-statistics, σ_i is approximately the low-statistics error. After dividing the χ^2 found between the simulated and experimental data sets by the degrees of freedom in the data, the reduced χ^2 is used as the metric for comparison between the two sets. If the initial template created falls under a desired significance - in this case a 2σ or 95% confidence interval - then the template created is established

to be a good fit to experiment. If the initial template fails fall within the confidence interval, then a different template is created using the spins, angular momenta, and mixing ratios for a different cascade, and the process is repeated until a good fit is found. A workflow for the goodness-of-fit process is shown in Figure 3.2.

For cascades containing a mixing ratio, templates were created for a range of mixing ratios for the specific cascade. Although mixing ratios vary between $-\infty$ and ∞, the values of the a_2 and a_4 coefficients converge for large $|\delta|$. Using this convergence, templates can be created where the mixing ratios simulated vary between of $-1 \leq \delta \leq 1$, as the most drastic changes in the angular coefficients caused by a variation in δ occur within this range. For a set of templates with a varied mixing ratio, the goodness-of-fit test was performed for each template in order to determine which mixing ratio provided the best fit to experiment.

The method of using templates to conduct a goodness-of-fit test was ultimately done to distinguish between spin states. A $2^+ \rightarrow 2^+ \rightarrow 0^+$ cascade with a mixing ratio of $\delta = 0.19$ has nearly the same values of angular correlation coefficients as a $4^+ \rightarrow 2^+ \rightarrow 0^+$ cascade with a $\delta = 0$ (Figure 3.3). In Andrew MacLean's thesis, templates were created for a number of ^{60}Co cascades, with the mixing ratio for the $2^+ \rightarrow 2^+ \rightarrow 0^+$ cascade varied around $\delta = 0.2$. After performing the goodness-of-fit test, taking the χ^2 statistic and dividing by the degrees of freedom to produce the reduced chi-square, a comparison of fit for each template against different confidence intervals was taken. The conclusions of this comparison can be seen in Figure 3.4, where it was found that $2^+ \rightarrow 2^+ \rightarrow 0^+$ at a measured mixing ratio of $\delta = 0.19$ could not be distinguished from $4^+ \rightarrow 2^+ \rightarrow 0^+$ at a mixing ratio of $\delta = 0$, as both cascades fall within the 2σ confidence interval.

Although using templates as a means to perform goodness-of-fit tests between the-
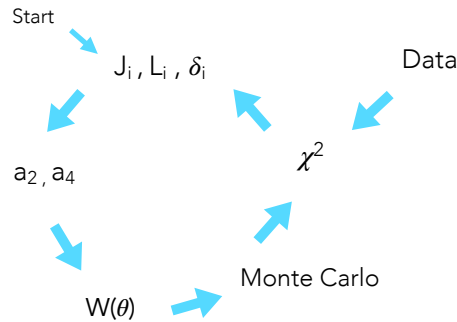
Figure 3.2: Goodness-of-fit workflow using the simulated angular correlation templates.
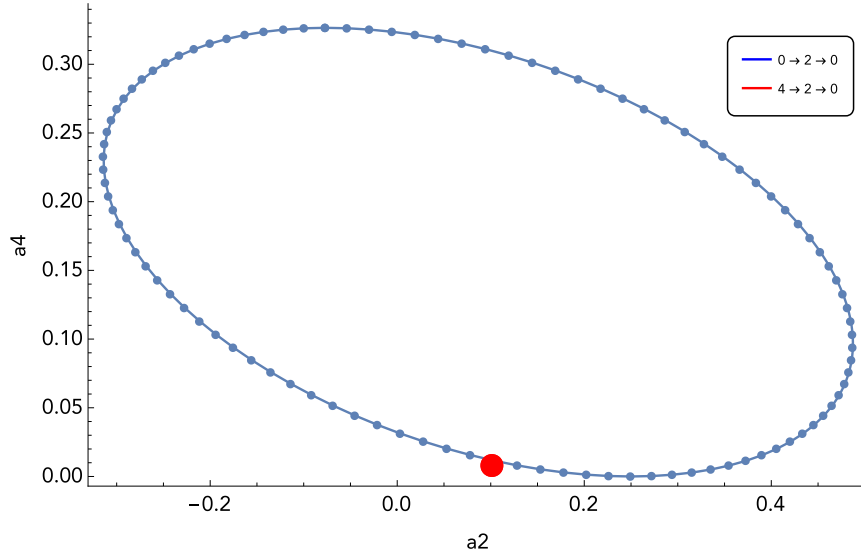
Figure 3.3: Elliptical plot of a_2 versus a_4 for a $2^+ \to 2^+ \to 0^+$ cascade (blue) and $4^+ \to 2^+ \to 0^+$ with $\delta = 0$ (red).

oretical and experimental angular correlations works well, the issue with this method stems from creating the templates themselves. Each template that corresponds to a particular cascade and multipolarity was created from a high-statistics simulation, where the information unique to the template was an input for the simulation. In order to create the template for the $4^+ \to 2^+ \to 0^+$ cascade, a simulation was run with the spins of the energy states set to $4^+, 2^+$, and 0^+, and the mixing ratio of the first γ-ray transition set to zero. To create the set of templates for the $2^+ \to 2^+ \to 0^+$ cascade, the mixing ratio of the first transition was varied between slightly around 0.2. Each of these simulations must be run for 10^9 events in order to reduce the error significantly, which takes roughly 20 computational days for a single template. Given the result of the goodness-of-fit test shown in Figure 3.4, 14 different templates were created in this plot alone, which amounts to a little more than nine months of running time. Not only is this process computationally expensive, but the task creating simulations for each particular cascade to be tested can prove to be an inconvenience to the experimental process; it is not uncommon to have tens of cascades to measure.

As a way to reduce the computation time needed for the goodness-of-fit method outlined here, the method of Reduced Simulation (RS) was created in order to make the data analysis process involving angular correlations more efficient. By using what is defined as the $\mathcal{Z}$ distribution in the following section, it is anticipated the RS method could streamline the data analysis process by only requiring three unique
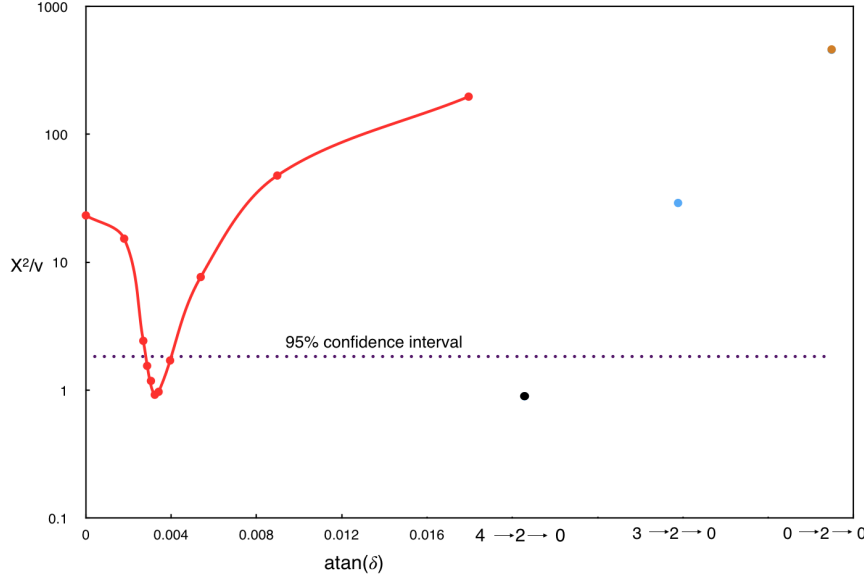
Figure 3.4: χ^2/ν versus $\arctan(\delta)$ for experimental ^{60}Co with a range of mixing ratios used for the $2^+ \rightarrow 2^+ \rightarrow 0^+$ cascade (red), and individual points for the $4^+2^+0^+$, $3^+2^+0^+$ and $0^+2^+0^+$ cascades. The $\operatorname{atan}(\delta)$ parameter on the left hand side of the x-axis is in terms of $\arctan(\delta \times \frac{pi}{180})$ [6].

simulations to produce any simulated angular correlation at those energies in the future.

3.2   The $\mathcal{Z}$ Distribution

The RS utilizes the linear combination of Legendre polynomials in $W(\theta)$ to create a set of three angular correlation simulations: one for P_0, one for P_2, and one for P_4. By doing so, these three distributions can then be appropriately weighted and added together to produce a new distribution: $\mathcal{Z}(\theta)$. To reiterate, the angular correlation between two γ rays is described by

$$W(\theta) = A_0[1 + a_2 P_2(\cos\theta) + a_4 P_4(\cos\theta)], \tag{3.3}$$

where P_2 and P_4 are the second and forth Legendre Polynomials and a_2 and a_4 are the physical angular correlation coefficients, as was described in Section 1.3. All Legendre polynomials have a range between -1 and 1, and $W(\theta)$ by definition must always be greater than zero for all θ in order to have a correct probability distribution. This condition makes it impossible to simulate the P_2 and P_4 components of an angular

correlation directly. However, by defining the following distributions:

$$\begin{aligned}
\mathcal{Z}_0(\theta) &= 1 \\
\mathcal{Z}_2(\theta) &= 1 + P_2(\cos\theta) \\
\mathcal{Z}_4(\theta) &= 1 + P_4(\cos\theta),
\end{aligned}$$
(3.4)

it becomes possible to simulate these polynomials individually. A linear combination of the distributions can be written as:

$$\begin{aligned}
x\mathcal{Z}_0(\theta) + y\mathcal{Z}_2(\theta) + z\mathcal{Z}_4(\theta) &= x + y + z + yP_2(\cos\theta) + zP_4(\cos\theta) \\
&= (x + y + z)\left[1 + \frac{y}{x+y+z}P_2(\cos\theta) + \frac{z}{x+y+z}P_4(\cos\theta)\right].
\end{aligned}$$
(3.5)

Comparing to Equation 3.4, the angular correlation coefficients then become:

$$A_0 = x + y + z$$
(3.6)

$$a_2 = \frac{y}{x+y+z}$$
(3.7)

$$a_4 = \frac{z}{x+y+z},$$
(3.8)

and the initial linear combination of distributions in Equation 3.5 can be written in terms of A_0, a_2, and a_4:

$$x\mathcal{Z}_0(\theta) + y\mathcal{Z}_2(\theta) + z\mathcal{Z}_4(\theta) = A_0[(1 - a_2 - a_4)\mathcal{Z}_0(\theta) + a_2\mathcal{Z}_2(\theta) + a_4\mathcal{Z}_4(\theta)].$$
(3.9)

This superposition of $\mathcal{Z}_0$, $\mathcal{Z}_2$, and $\mathcal{Z}_4$ is defined as the $\mathcal{Z}$ distribution.

The crux of understanding the significance behind the $\mathcal{Z}$ distribution and its role in the RS method is its connection to the angular correlation function, $W(\theta)$. As was described previously, a simulation for any $\gamma - \gamma$ cascade begins with the theoretical $W(\theta)$ distribution, which is determined from the calculated values for a_2 and a_4. From here, this distribution is fed into a Monte Carlo simulation where is it is reproduced as a slightly different distribution that contains the alterations due to the efficiency, finite resolution, and geometric effects of the detector. The $\mathcal{Z}$ distribution, being composed of a linear combination of simulated Legendre polynomials, already contains the effects of the detector. In order to produce a simulated data set for a specific cascade, the only necessary step is to calculate a_2 and a_4 and input the values
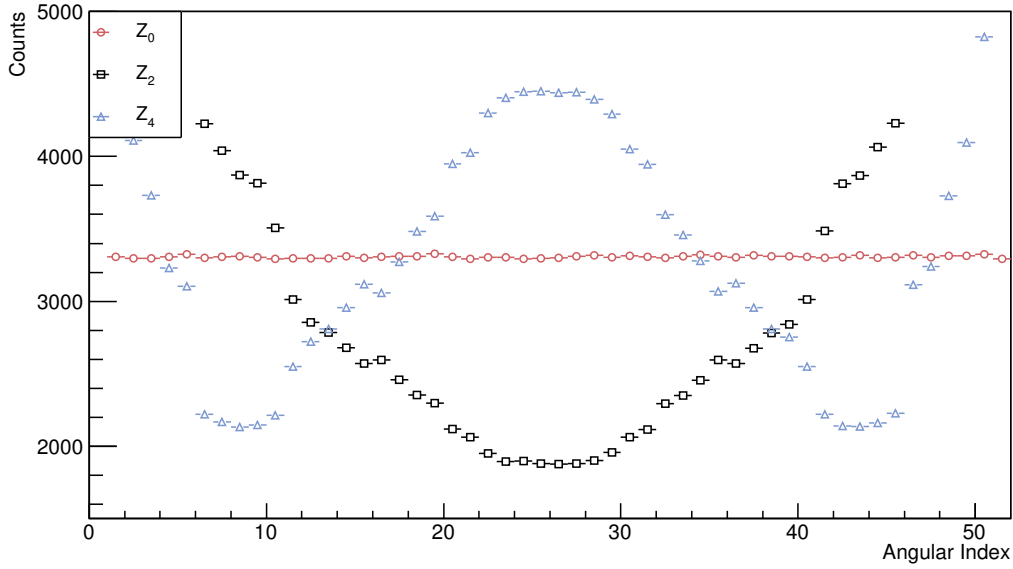
Figure 3.5: Simulated $\mathcal{Z}_0$ (red), $\mathcal{Z}_2$ (black), and $\mathcal{Z}_4$ (blue) distributions at 10^9 events.

into Equation 3.9. In contrast to the goodness-of-fit method outlined in the previous section, the step of simulating each template defined by its $W(\theta)$ function is eliminated, as the $\mathcal{Z}$ distribution can reproduce any simulated angular correlation simply by scaling and adding the individual components of the $\mathcal{Z}$ distribution appropriately.

Once the $\mathcal{Z}$ distribution is created by simulating the three individual components, the goodness-of-fit test can be performed simply by varying the physical values of a_2 and a_4 corresponding to different angular correlations in order to produce the simulated data to be compared to experiment. As the building blocks of each simulated data set produced by $\mathcal{Z}$ are only three simulations - $\mathcal{Z}_0$, $\mathcal{Z}_2$, and $\mathcal{Z}_4$ - the running time to perform a goodness-of-fit test is roughly 45 days for *any* number of cascade comparisons.

The simulated $\mathcal{Z}_0$, $\mathcal{Z}_2$, and $\mathcal{Z}_4$ distributions are shown in Figure 3.5. The technique used to create these Legendre distributions is further described in Appendix A.

3.3   Proof of Concept

The RS method was first tested to determine the accuracy at which the $\mathcal{Z}$ distribution could create simulated angular correlations, and was ultimately proven to work as a basis for the goodness-of-fit test. In order to demonstrate the correspondence between the angular correlations produced using the $\mathcal{Z}$ distribution and the angular correla-
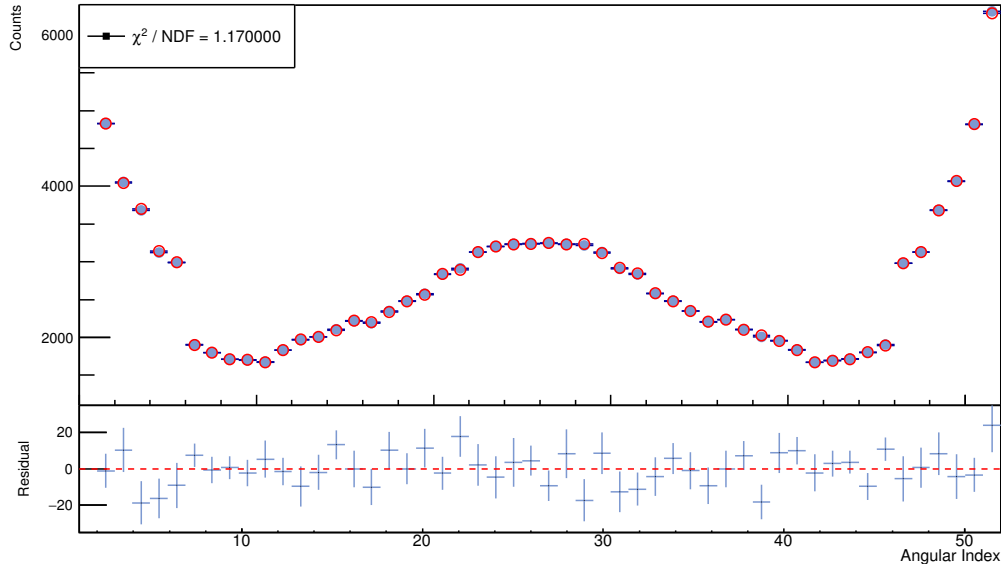
Figure 3.6: Normalized $0^+ \rightarrow 2^+ \rightarrow 0^+$ angular index histograms for simulated experimental data (solid blue) and constructed data using the RS method (open red), along with the residual. The reduced chi-square between the histograms was found to be 1.17.

tions simulated individually, angular correlation histograms were created in terms of angular index using both methods for a $0^+ \rightarrow 2^+ \rightarrow 0^+$ cascade, and overlaid over one another, as shown in Figure 3.6. Here, the residual between the two data sets is also displayed, where the difference statistically agrees with zero for a majority of angular indices. The residual, combined with the χ^2/ν of 1.17, indicates a statistical equivalence between the two angular correlations. This process of comparing recreated to individually simulated data was repeated for a number of different cascades, with the reduced chi-square between each method shown in Table 3.2.

Knowing the angular correlations created using the RS method successfully re-

Cascade	χ^2/ν
$4^+ \rightarrow 2^+ \rightarrow 0^+$	1.74
$0^+ \rightarrow 2^+ \rightarrow 0^+$	1.17
$1^+ \rightarrow 2^+ \rightarrow 0^+$	1.59
$3^+ \rightarrow 2^+ \rightarrow 0^+$	1.32
$2^+ \rightarrow 2^+ \rightarrow 0^+ (\delta = 0.19)$	1.66

Table 3.2: Reduced chi-squares between individually simulated and recreated angular correlations using the RS method.
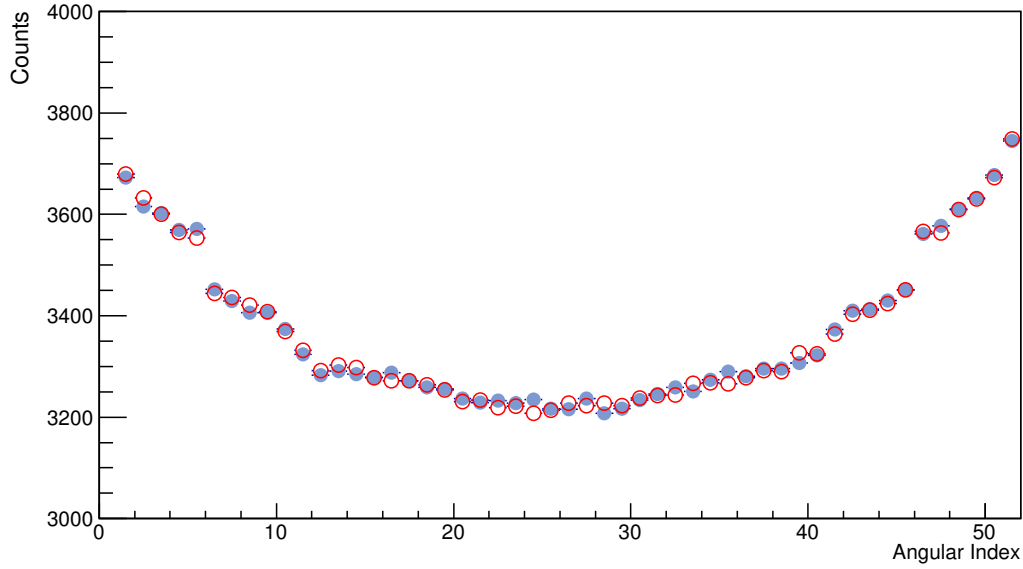
Figure 3.7: Normalized $4^+ \rightarrow 2^+ \rightarrow 0^+$ angular index histograms for simulated experimental data (solid blue) and best fit using the RS method (open red).

produce individually simulated angular correlations, they were then used to perform goodness-of-fit tests against low-statistics simulated angular correlations, in order to replicate experimental data. As was described earlier, the reduced chi-square is the metric by which simulated data is compared to experimental measurement. In order to calculate this metric, the $\mathcal{Z}$ distribution was used as a fit to low-statistics simulated data, where the $\mathcal{Z}_0$, $\mathcal{Z}_2$, and $\mathcal{Z}_4$ distributions were scaled to the data using the physical a_2 and a_4 coefficients as the fit parameters defined in Equation 3.9. The fit was performed by keeping both the $\mathcal{Z}$ distribution and experimental data in the form of a normalized angular index histogram to ensure that the angular correlation was scaled appropriately. By using this method of fitting histograms to histograms, the $\mathcal{Z}$ distribution is automatically reshaped to create the best fit to data, without the prior knowledge of the initial a_2 and a_4 coefficients. In turn, this fit allowed for a direct measurement of the angular coefficients found in the simulated data, as a_2 and a_4 are used as the fitting parameters. The use of this method is illustrated in Figure 3.7, where an experimental $4^+ \rightarrow 2^+ \rightarrow 0^+$ cascade is fit using the $\mathcal{Z}$ distribution. Here, solid blue circles represent experimental data, while the open red circles represent the best fit to the data at a $\chi^2/\mathrm{NDF} = 1.66$.

   Using the the RS method, the simulated $0^+ \rightarrow 2^+ \rightarrow 0^+$ cascade was fit with the $\mathcal{Z}$ distribution in order to extract the measured a_2 and a_4 coefficients. In comparison

Coefficient	Physical	Measured
a_2	0.3571428	0.3571 ± 0.0003
a_4	1.1428571	1.142 ± 0.001

Table 3.3: Physical and measured angular coefficients for a $0^+ \rightarrow 2^+ \rightarrow 0^+$ cascade at $\delta = 0$ using the RS method.

to the angular correlation coefficients found from fitting this cascade with a line (Table 3.1), the coefficients measured using this method agree with the theoretical coefficients of the $0^+ \rightarrow 2^+ \rightarrow 0^+$ cascade (Table 3.3).

As scaling the $\mathcal{Z}$ distribution allows for a quick and efficient fit to experimental data, performing a goodness-of-fit test for a number of different cascades becomes relatively easy. Specifically, finding the reduced chi-square to distinguish between spin states only requires varying the $\mathcal{Z}$ distribution, rather than individually simulating each angular correlation to be tested against experimental data. For a given experimental data set, performing the goodness-of-fit begins by first choosing the spins, angular momenta, and mixing ratios for the cascade to be tested, and then calculating the theoretical a_2 and a_4 coefficients. The $\mathcal{Z}$ distribution is then scaled appropriately using the coefficients, and the reduced chi-squared is taken between the distribution and the experimental data. Similar to the method that uses the angular correlation templates, if the chi-square statistic fails to fall below a desired confidence interval, then a new cascade is chosen, and the process repeats until a good fit is found. In contrast to the workflow illustrated in Figure 3.2, the goodness-of-fit process is visualized in Figure 3.8. Here, the efficiency of the RS method is emphasized in the new workflow, where the simulation step lies outside of the sequence loop.

To demonstrate the utility of the RS method, the result from Figure 3.4 was recre-
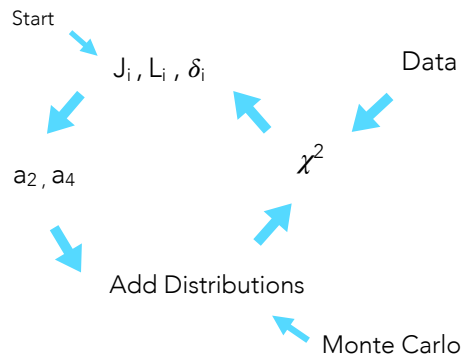

Figure 3.8: Goodness-of-fit workflow using the RS method.
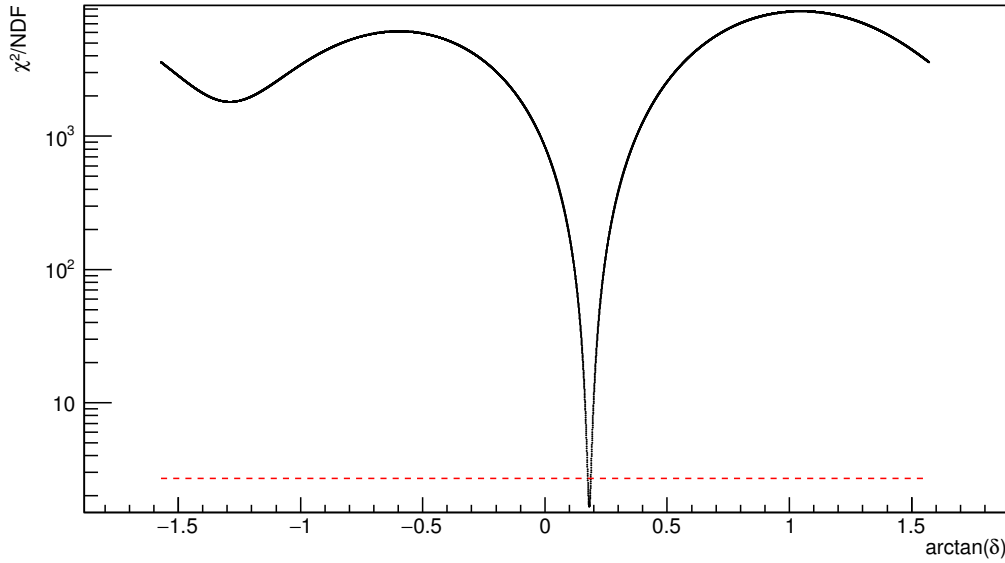
Figure 3.9: Goodness-of-fit for the $2^+ \rightarrow 2^+ \rightarrow 0^+$ cascade to simulated data, with the mixing varied from $\arctan(\delta)$ from $-\frac{\pi}{2} \rightarrow \frac{\pi}{2}$ in 10000 steps. The dashed red line indicates the 2σ limit. While, this plot was created for comparison with the red line in Figure 3.4, it also can be compared to same cascade shown in Figure 1.4.

ated. The goodness-of-fit was taken for the $2^+ \rightarrow 2^+ \rightarrow 0^+$ cascade to experimental data, where the mixing ratio was varied between 0 and 1 to create 11 different cascades for comparison. To perform the same fit using the RS method, the theoretical coefficients for the 11 cascades used in the comparison would need to be calculated in order to produce the corresponding angular correlations using the $\mathcal{Z}$ distribution, which would then be fit to the experimental data. However, because any angular correlation can be produced using the $\mathcal{Z}$ distribution, the goodness-of-fit in Figure 3.4 can be improved by introducing more angular correlations to be compared to data. As was mentioned before, the mixing ratio for any cascade varies between $-\infty$ and ∞. Rather than sample δ between -1 and 1, sampling $\arctan(\delta)$ from $-\frac{\pi}{2} \rightarrow \frac{\pi}{2}$ ensures an more even distribution of the mixing ratio. With this sampling in mind, the plot in Figure 3.4 was recreated by varying the $\arctan(\delta)$ for the $2^+ \rightarrow 2^+ \rightarrow 0^+$ cascade from $-\frac{\pi}{2}$ to $\frac{\pi}{2}$ in increments of $\frac{\pi}{10000}$. In turn, this produced 10000 different angular correlations to be compared to experiment. The resulting goodness-of-fit is shown in Figure 3.9, where the line is composed of 10000 points, and the dashed red line is the 2σ confidence limit. The minima in the fit corresponds to a reduced chi-square of 1.66266, which corresponds to a mixing ratio of 0.19, as expected. Should each of the 10000 angular correlations have been individually simulated, creating this plot
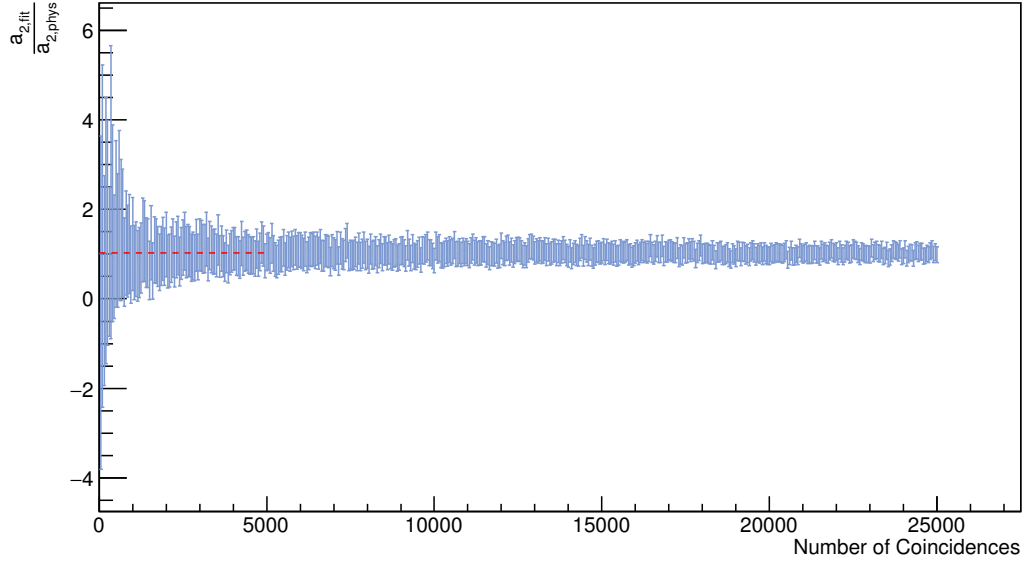
Figure 3.10: Ratio of measured ($a_{2,fit}$) and physical ($a_{2,phys}$) with associated error for number of histograms with increasing events. The dashed red line indicates the ratio convergence at a value of 1.02 ± 0.04.

would have taken 200000 days, or nearly 550 years. Instead, the simulations needed to create the $\mathcal{Z}$ distribution - and corresponding points on Figure 3.9 - took only 60 days[2].

3.4 Limits

Once the validity of the RS method for reproducing a goodness-of-fit was tested, limits were taken to see how many events in an experimental data set were needed in order for the $\mathcal{Z}$ distribution to provide an accurate fit. To show this, a simulated angular correlation for a $4^+ \rightarrow 2^+ \rightarrow 0^+$ cascade was created for 10^9 events. Due to the resolution properties of GRIFFIN, only a fraction of the emitted γ rays are actually measured by the detector, and a high-statistics angular correlation histogram only contains 2.5×10^7 events. From here, a set of lower-statistics angular correlations for the $4^+ \rightarrow 2^+ \rightarrow 0^+$ cascade were made by creating histograms filled with a smaller number of events using the same distribution found from the high-statistics histogram. The $\mathcal{Z}$ distribution was then used to fit each lower-statistics histogram to produce measured a_2 and a_4 coefficients. As the values of the measured and theoretical angular

---

[2]It should be noted here that although this process takes 60 days computationally, high-speed computers with multiple cores does speed this process up considerably.

coefficients should agree using the $\mathcal{Z}$ distribution, the ratio between the two values for a_2 was taken at each lower-statistic histogram as a measure of fit. As Figure 3.10 shows, as the number events increases the ratio between the coefficients converges to 1.02, with the limiting factor on the error being the fitted value of a_2. Given this result, the number of events for an experimental angular correlation spectrum should be above 15000 in order for the $\mathcal{Z}$ distribution to be accurate to the order of 10^{-3}.

Chapter 4

Linear Approximation of $\mathcal{Z}$

In the previous chapter, the Reduced Simulation (RS) method was defined for fitting experimental angular correlations using the $\mathcal{Z}$ distribution: a superposition of three simulated Legendre Polynomials of orders 0, 2 and 4. Here, rather than using the $\mathcal{Z}$ distribution to reproduce angular correlation simulations, an argument is made for the use of algebraic expressions to calculate the angular coefficients that would normally be measured in simulation or experiment. By using these calculations, angular correlations measured from simulated data can be reproduced analytically.

4.1   Background

The center piece of the RS method is the $\mathcal{Z}$ distribution, which is composed of the three individual distributions:

$$
\begin{aligned}
\mathcal{Z}_0 &= 1 \\
\mathcal{Z}_2 &= 1 + P_2(\cos\theta) \\
\mathcal{Z}_4 &= 1 + P_4(\cos\theta).
\end{aligned}
\tag{4.1}
$$

After these distributions are simulated, an angular correlation can be recreated by scaling the distributions and adding them appropriately using the theoretical a_2 and a_4 coefficients for a given cascade. However, the individual $\mathcal{Z}$ distributions, once simulated, never change. The same three distributions are simply used repeatedly as the basis elements for the creation of simulated angular correlations. Because the distributions themselves are fixed in the analysis process, it follows that a line fit to the simulated distributions would also be fixed. Using this logic, it then becomes possible to approximate the distributions in terms of a set of functions, namely the

(a)   (b)

(c)
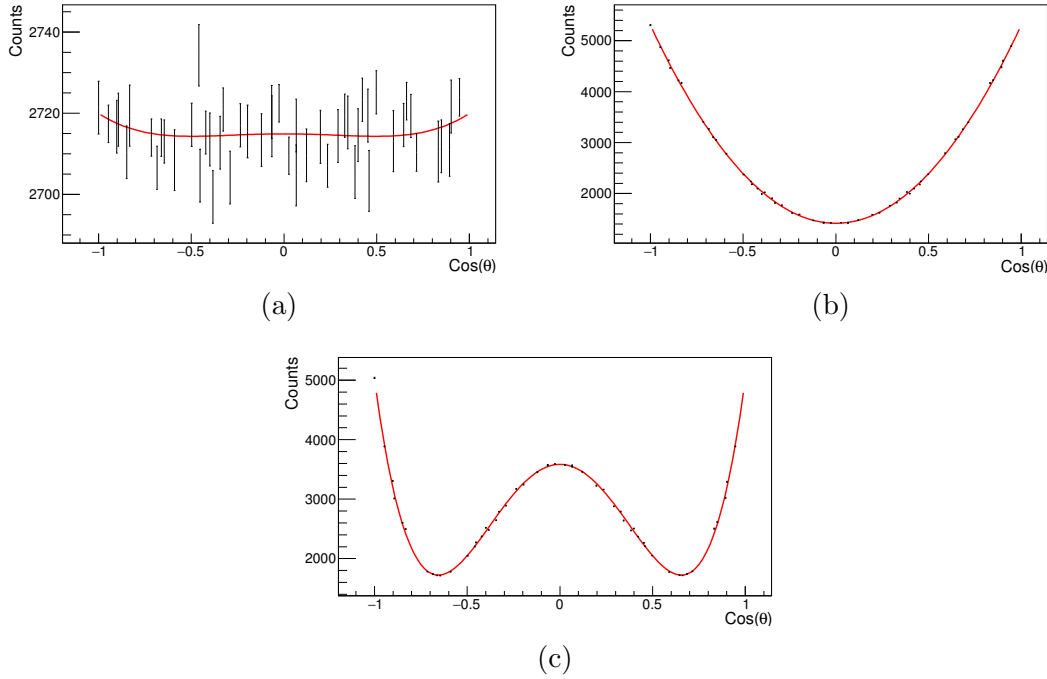
Figure 4.1: Individually simulated $\mathcal{Z}_0$ (a), $\mathcal{Z}_2$ (b), and $\mathcal{Z}_4$ (c) distributions fit with a $W(\theta)$ function (shown in red).

angular correlation function $W(\theta)$, by fitting $W(\theta)$ to each distribution. Figure 4.1 shows the result of these fits, where the red line in each simulated distribution is the respective $W(\theta)$ fit. Ultimately, the individual $\mathcal{Z}$ distributions become delineated by the coefficients of their respective functions, as the unique shape of an angular correlation function is given by its a_2 and a_4 coefficients.

Previously, the RS method was first shown to accurately reproduce simulated angular correlations, where in addition to overlaying histograms and running a reduced chi-square between the two methods, the measured angular correlation coefficients from an individually simulated $0^+ \rightarrow 2^+ \rightarrow 0^+$ cascade (c_2 and c_4) matched the measured coefficients from the same cascade made using the RS method. Here, the measured coefficients were determined by fitting the histograms with a $W(\theta)$ function. In a different process that involved fitting individually simulated histograms with histograms made via the $\mathcal{Z}$ distribution, angular correlation coefficients were extracted from the simulated data that more closely agreed with the physical coefficients (a_2 and a_4). This method was shown to work, as the $\mathcal{Z}$ distribution contained the distorting effects caused by the GRIFFIN detectors. In the following section, using the approximation of the $\mathcal{Z}$ distribution in the angular correlation data analysis

process is further explored by testing its ability to both recreate angular correlations and extract accurate angular correlation coefficients.

4.2 Proof of Concept

The individual $\mathcal{Z}$ distributions are approximated by re-defining them as separate $W(\theta)$ functions:

$$
\begin{aligned}
\mathcal{Z}_0 \rightarrow \mathcal{L}_0 &= \alpha_0(1 + \alpha_2 P_2 + \alpha_4 P_4) \\
\mathcal{Z}_2 \rightarrow \mathcal{L}_2 &= \beta_0(1 + \beta_2 P_2 + \beta_4 P_4) \\
\mathcal{Z}_4 \rightarrow \mathcal{L}_4 &= \gamma_0(1 + \gamma_2 P_2 + \gamma_4 P_4),
\end{aligned}
\tag{4.2}
$$

with α, β, and γ being the coefficients that delineate each function, respectively. As was described in Chapter 3, the $\mathcal{Z}$ distribution is created from a linear combination of the individual distributions using the physical a_2 and a_4 coefficients (Equation 3.9). Using the approximated $\mathcal{L}$ distributions, the $\mathcal{Z}$ distribution then becomes:

$$
\mathcal{Z} \approx (1 - a_2 - a_4)\mathcal{L}_0 + a_2\mathcal{L}_2 + a_4\mathcal{L}_4
$$

$$
= (1 - a_2 - a_4)[\alpha_0(1 + \alpha_2 P_2 + \alpha_4 P_4)] + a_2[\beta_0(1 + \beta_2 P_2 + \beta_4 P_4)] + a_4[\gamma_0(1 + \gamma_2 P_2 + \gamma_4 P_4)]
$$

$$
= N[(1 - a_2 - a_4)(1 + \alpha_2 P_2 + \alpha_4 P_4) + a_2(1 + \beta_2 P_2 + \beta_4 P_4) + a_4(1 + \gamma_2 P_2 + \gamma_4 P_4)]
\tag{4.3}
$$

Here, it becomes important to note that the normalization coefficients - α_0, β_0, and γ_0 - are roughly equal to one another, as shown in Table 4.1. This equivalence allows for a simplification of the approximation of $\mathcal{Z}$, where N is defined to be $\alpha_0 = \beta_0 = \gamma_0$. Continuing the approximation, where:

$$
\mathcal{Z} \approx N[1 + (\alpha_2 - a_2\alpha_2 - a_4\alpha_2 + a_2\beta_2 + a_4\gamma_2)P_2 + (\alpha_4 - a_2\alpha_4 - a_4\alpha_4 + a_2\beta_4 + a_4\gamma_4)P_4]
$$

$$
\equiv N[1 + c_2 P_2 + c_4 P_4],
\tag{4.4}
$$

for

$$
c_2 = \alpha_2 - a_2(\alpha_2 - \beta_2) - a_4(\alpha_2 - \gamma_2),
\tag{4.5}
$$

and

$$c_4 = \alpha_4 - a_2(\alpha_4 - \beta_4) - a_4(\alpha_4 - \gamma_4). \tag{4.6}$$

Referring back to Chapter 3, the $\mathcal{Z}$ distribution was scaled using the physical a_2 and a_4 coefficients in order to recreate simulated angular correlations. In turn, a $W(\theta)$ function was fit to these recreated angular correlations and was compared to fits from individually simulated angular correlations, where the fitted c_2 and c_4 angular correlation coefficients agreed between the two sets, as indicated by the reduced chi-square values in Table 3.2. Notably, the RS method was used to create angular correlations of the form:

$$\mathcal{Z}(\theta) \propto 1 + c_2 P_2(\cos\theta) + c_4 P_4(\cos\theta) \tag{4.7}$$

When compared to Equation B.2, the c_2 and c_4 coefficients found from the approximation of $\mathcal{Z}$ should be same as the c_2 and c_4 coefficients measured by fitting the angular correlations created using the RS method, as both methods rely the physical a_2 and a_4 coefficients to produce fitted coefficients. Only with the approximation, the fit is first performed on the individual $\mathcal{Z}$ distributions with the coefficients scaled appropriately, rather than using first using the $\mathcal{Z}$ distribution to create the simulated angular correlation to be fit. As a result, the approximation of $\mathcal{Z}$ allows c_2 and c_4 to be calculated analytically using the α, β, and γ coefficients.

In order to determine the values of the coefficients for the approximated $\mathcal{Z}$ distribution, each of the three individual distributions was fit with an angular correlation function $W(\theta)$, according to Equation B.1 (Figure 4.1). The approximation coefficients produced from the best fit are shown in Figure 4.1.

Given the the individual $\mathcal{Z}$ distributions, the values of the coefficients in Table 4.1 are in agreement with Equation 4.1, as it should be expected that $\beta_2 \approx \gamma_4 \approx 1$, and the remaining coefficients ≈ 0. Using the α, β, and γ coefficients, the calculated values for c_2 and c_4 given by Equations B.4 and B.5 become:

$$\tilde{c}_2 = 0.9545 a_2 - 0.0052 a_4 + 0.0009, \tag{4.8}$$

and

$$\tilde{c}_4 = 0.8503 a_4 - 0.0023 a_2 + 0.0008, \tag{4.9}$$

where the tilde denotes an analytically calculated coefficient, and a_2 and a_4 are the physical coefficients. Here, it become important to notice that both Equations 4.8 and 4.9 are weakly coupled to one another; $\tilde{c}_2$ and $\tilde{c}_4$ are dependent on both physical

| coeff.	value	error
α_0	2713.6	0.8
α_2	0.0009	0.0007
α_4	0.0008	0.0009
β_0	2713.6	0.8
β_2	0.9556	0.0007
β_4	-0.001	0.001
γ_0	2713.6	0.8
γ_2	-0.0043	0.0008
γ_4	0.8512	0.0009

Table 4.1: Coefficient values for the approximated $\mathcal{Z}$ distribution of a 1173-1332 keV cascade, as described by Equation B.1.

coefficients. In order to determine the relationship between the calculated angular coefficients and the coefficients produced from fitting $W(\theta)$ to data, the values for the two types of coefficients were first found for a number of different cascades. Using the RS method, simulated cascades were produced from physical a_2 and a_4 coefficients, which were then fit to extract c_2 and c_4. For each angular correlation made using the $\mathcal{Z}$ distribution, the approximated $\mathcal{Z}$ was also used to calculate $\tilde{c}_2$ and $\tilde{c}_4$. The calculated coefficients were then plotted against the fitted coefficients, with the results shown in Figure 4.2 (a) and 4.2 (b). Here, the ratio of $\tilde{c}_2$ against c_2 was found to be 1.0011 ± 0.0004, while the ratio of $\tilde{c}_4$ against c_2 was found to be 1.0012 ± 0.0009. In addition to using the angular correlations made via the RS method, the same process of finding the ratios between the calculated and fitted coefficients was performed using individually simulated angular correlations. The results using the individual angular correlations are found in Figure 4.3 (a) and 4.3 (b), where the ratio between $\tilde{c}_2$ and c_2 was found to be 1.001 ± 0.003, and the ratio between $\tilde{c}_4$ and c_4 was found to be 1.001 ± 0.002. Remarkably, these results demonstrates the ability of the $\mathcal{Z}$ approximation to analytically determine the coefficients that would otherwise be found from a fit to simulated data. Furthermore, the feature of the ratios between calculated and measured coefficients taken from different methods of angular correlation being in statistical agreement is a favorable result that further illustrates the ability of the RS method to recreate simulated angular correlations.

It should be noted here that the fit used to determine these ratios was the slope of the fitted lines in Figure 4.2, where the offset of the line was forced to 0. With the
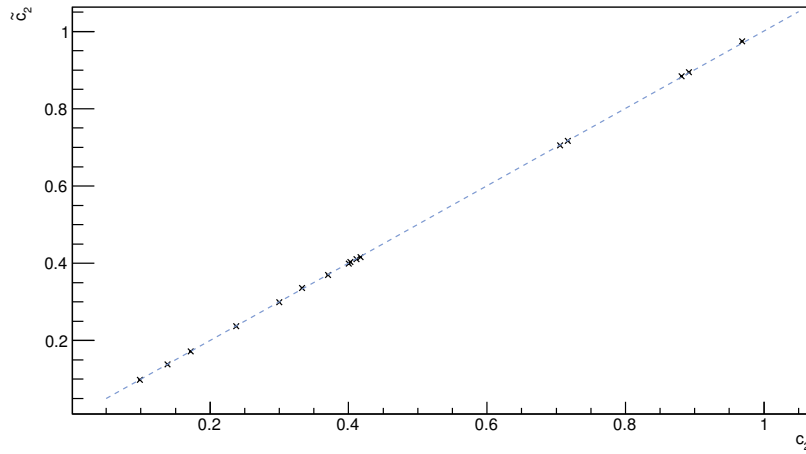
(a)
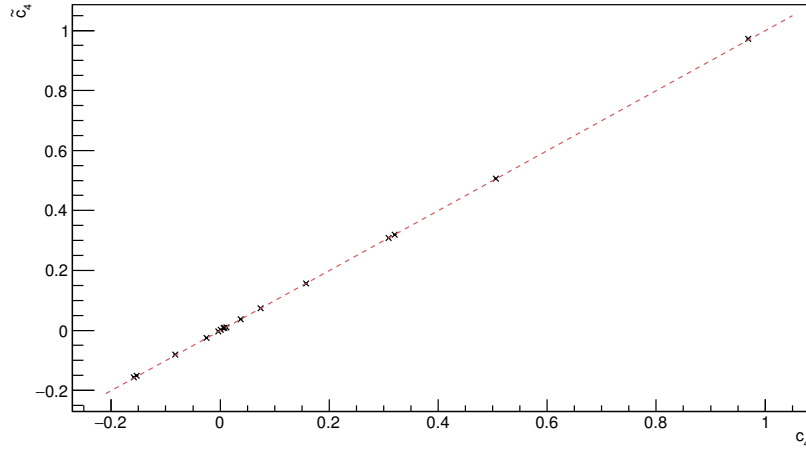
(b)

Figure 4.2: Calculated versus measured angular correlation coefficients for a number of angular correlations produced using the RS method. The slope between the $\tilde{c}_2$ and c_2 coefficients was found to be 1.0011 ± 0.0004, given by the blue dashed line (a), while the slope between the $\tilde{c}_4$ and c_4 coefficients was found to be 1.0012 ± 0.0009, given by the red dashed line (b).

offset able to float freely durring a fit, the fitted lines the figure become:

$$\tilde{c}_2 = 1.0037(\pm 0.0004)a_2 - 0.002(\pm 0.0005)$$
$$\tilde{c}_4 = 1.001(\pm 0.002)a_4 - 0.005(\pm 0.007)$$
$$(4.10)$$

The offsets produced from these fits originate from the coupled nature of Equations 4.8 and 4.9. For example, the calculation of $\tilde{c}_2$ depends on both a_2 and a_4. In
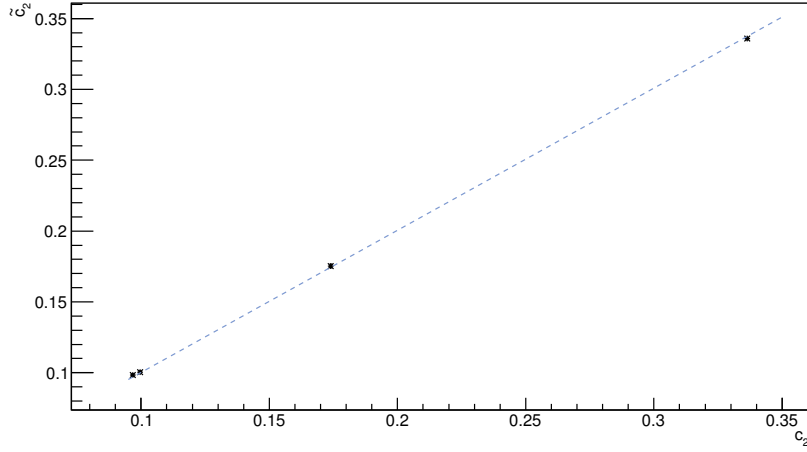
(a)
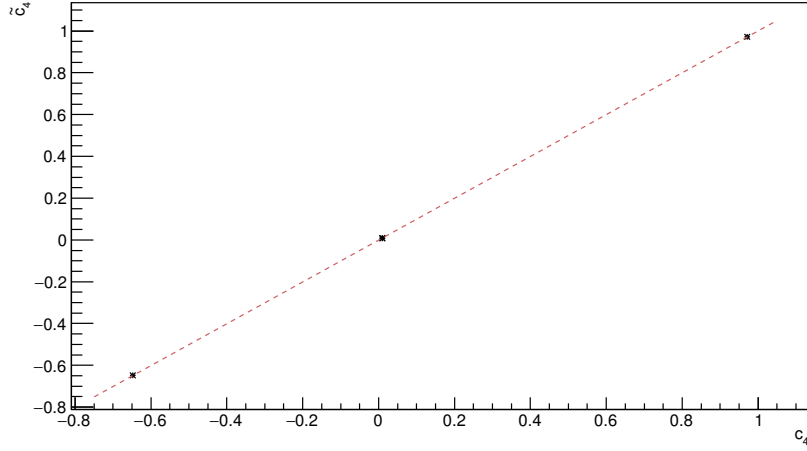
(b)

Figure 4.3: Calculated versus measured angular correlation coefficients for a number of individually simulated angular correlations. The slope between the $\tilde{c}_2$ and c_2 coefficients was found to be 1.001 ± 0.003, given by the blue dashed line (a), while the slope between the $\tilde{c}_4$ and c_4 coefficients was found to be 1.001 ± 0.002, given by the red dashed line (b).

terms of the fitted line of $\tilde{c}_2$ against a_2, a_4 contributes to the offset of the line. For angular correlations with larger values of a_4, the offset of the ratio between $\tilde{c}_2$ and c_2 will become larger. The effect of this can be seen in Figure 4.4. Here, the a_2 coefficient was chosen to be 0.1 and the a_4 coefficient was given two values: 0.2 and 0.01. Using Equations 4.8 and 4.9, this produced two sets of different calculated $\tilde{c}_2$ and $\tilde{c}_4$ coefficients: 0.09532 and 0.17068 for $a_4 = 0.2$, and 0.09631 and 0.00911 for $a_4 = 0.01$, respectively. These calculated coefficients were then used to create
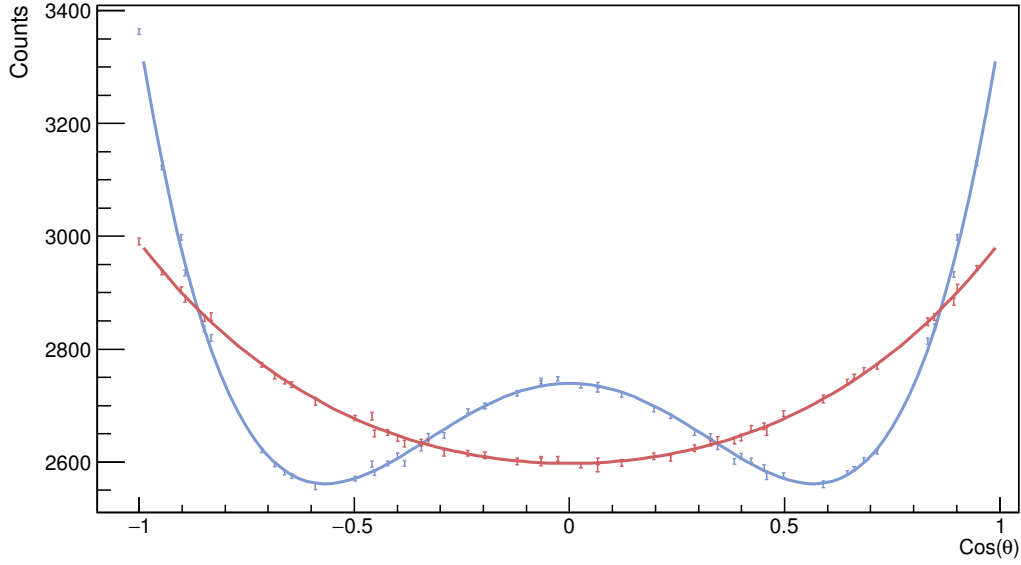
Figure 4.4: Two simulated angular correlations producing using the approximated $\mathcal{Z}$ distribution using a single value of $a_2 = 0.1$, and an $a_4 = 0.2$ (blue) and $a_4 = 0.01$ (red).

the simulated angular correlations shown in Figure 4.4 in order to demonstrate the particular ability of the approximated $\mathcal{Z}$ distribution to create two distinct data sets from a single a_2 value.   As was mentioned earlier, in addition to checking the ability of the approximated $\mathcal{Z}$ distribution to reproduce the measured c_2 and c_4 coefficients, the method was also tested to determine whether or not the approximation could be used to extract accurate angular correlation coefficients that more closely agree with the physical coefficients of a particular cascade. Looking back to Equations B.4 and B.5, where

$$c_2 = \alpha_2 - a_2(\alpha_2 - \beta_2) - a_4(\alpha_2 - \gamma_2) \tag{4.11}$$

$$c_4 = \alpha_4 - a_2(\alpha_4 - \beta_4) - a_4(\alpha_4 - \gamma_4), \tag{4.12}$$

these are functions of the physical coefficients a_2 and a_4 that analytically produce what would be the measured coefficients: c_2 and c_4. To analytically calculate the measured coefficients that more closely resemble physical coefficients rather than the measured coefficients containing the effects of the detector, the above equations were
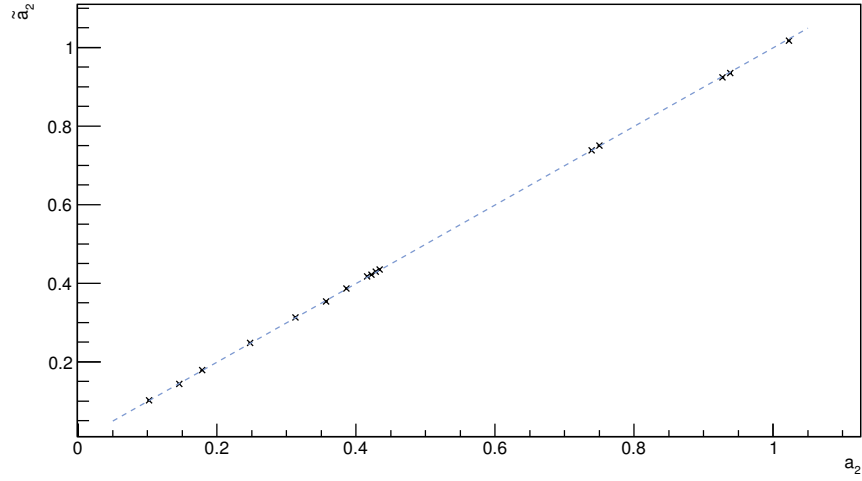
(a)
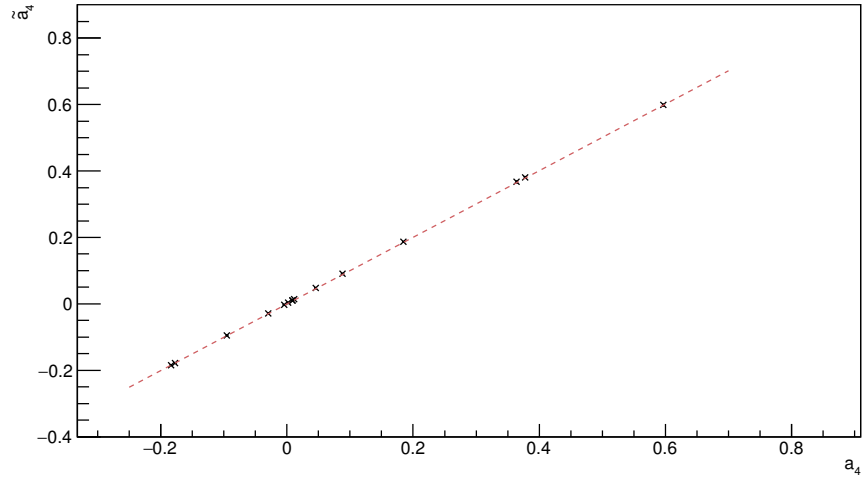
(b)

Figure 4.5: Calculated versus physical angular correlation coefficients for a number of angular correlations produced using the RS method. The slope between the $\tilde{a}_2$ and a_2 coefficients was found to be 0.999 ± 0.003, given by the blue dashed line (a), while the slope between the $\tilde{a}_4$ and a_4 coefficients was found to be 1.001 ± 0.002, given by the red dashed line (b).

rewritten[1] in order to have a_2 and a_4 in terms of c_2 and c_4:

$$a_2 = \frac{\frac{(c_2-\alpha_2)(\alpha_4-\gamma_4)}{\alpha_2-\gamma_2} - c_4 + \alpha_4}{\frac{(\alpha_2-\beta_2)(\alpha_4-\gamma_4)}{\alpha_2-\gamma_2} + \alpha_4 - \beta_4} \tag{4.13}$$

---

[1]A more rigorous algebraic derivation can be found in Appendix B.
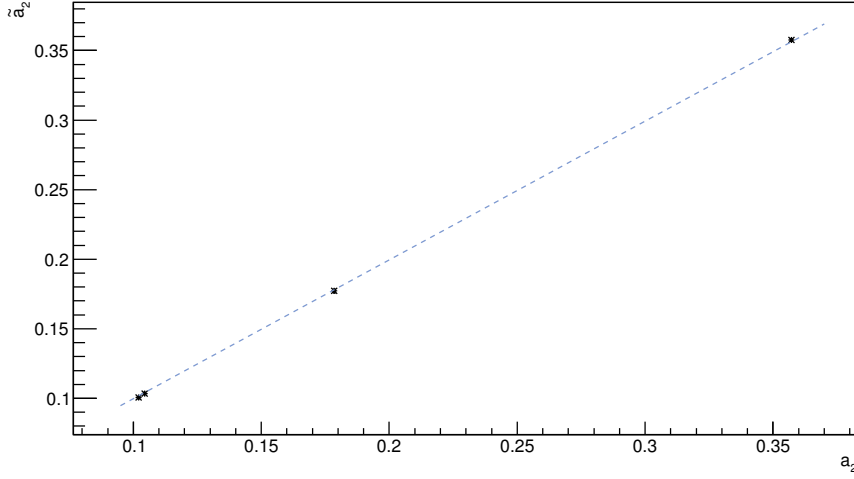
(a)
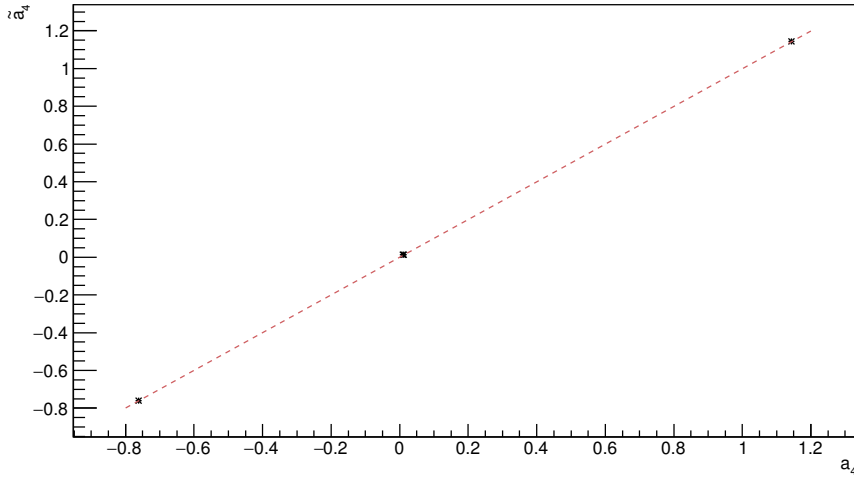
(b)

Figure 4.6: Calculated versus physical angular correlation coefficients for a number of individually simulated angular correlations. The slope between the $\tilde{a}_2$ and a_2 coefficients was found to be 0.987 ± 0.002, given by the blue dashed line (a), while the slope between the $\tilde{a}_4$ and a_4 coefficients was found to be 1.001 ± 0.003, given by the red dashed line (b).

$$a_4 = \frac{\frac{(c_2 - \alpha_2)(\alpha_4 - \beta_4)}{\alpha_2 - \beta_2} - c_4 + \alpha_4}{\frac{(\alpha_2 - \gamma_2)(\alpha_4 - \beta_4)}{\alpha_2 - \beta_2} + \alpha_4 - \gamma_4}. \tag{4.14}$$

In terms of the measured values for the α, β, and γ coefficients, these equations then become:

$$\tilde{a}_2 = 1.0475c_2 + 0.0064c_4 - 0.0009, \tag{4.15}$$

and,

$$\tilde{a}_4 = 1.1760c_4 + 0.0028c_2 + 0.0010, \tag{4.16}$$

where the tilde again denotes an analytically calculated coefficient, while c_2 and c_4 are the measured angular correlation coefficients from a simulated or experimental data set containing the detector effects.

In a similar process used to determine the relationship between $\tilde{c}_2/\tilde{c}_4$ and c_2/c_4, the angular correlation coefficients $\tilde{a}_2$ and $\tilde{a}_4$ were calculated for a number of different cascades and compared to their physical coefficient counterparts. The RS method was first used to create simulated angular correlations from the physical a_2 and a_4 coefficients, which were then fit using a $W(\theta)$ function to extract the measured c_2 and c_4 coefficients. For each simulated angular correlation, $\tilde{a}_2$ and $\tilde{a}_4$ were calculated using the respective c_2 and c_4 coefficients. The calculated coefficients were then plotted against the physical coefficients, with the results shown in Figure 4.5. Here, the slope of the fitted line for $\tilde{a}_2$ against a_2 was found to be 0.999 ± 0.003, while the slope of the fitted line for $\tilde{a}_4$ against a_4 was found to be 1.001 ± 0.002. Additionally, the process was repeated using individually simulated angular correlations, rather than constructing the simulations using the $\mathcal{Z}$ distribution. The results for this method are shown in Figure 4.6, where the slope of the fitted line for $\tilde{a}_2$ against a_2 was found to be 0.987 ± 0.002, while the slope of the fitted line for $\tilde{a}_4$ against a_4 was found to be 1.001 ± 0.003.

Calculating the $\tilde{a}_2$ and $\tilde{a}_4$ coefficients for both angular correlations produced using the RS method and those individually simulated gave the same result of a one-to-one relationship between each of the two values. Although this result itself is useful, as the approximated $\mathcal{Z}$ distribution was able to accurately produce angular correlation coefficients that have the detector effects removed analytically, there exists an underlying utility. Experimentalists working with either experimental or simulated angular correlations will now be able to fit the data with a $W(\theta)$ function, measure the c_2 and c_4 coefficients, and then feed the measured coefficients into Equations 4.15 and 4.16 in order to extract the angular correlation coefficients that closely resemble the physical values. Fitting the data with simulations is no longer required, as this process can be accomplished analytically.

4.3   Limits

Finally, as was done in the preceding chapter, limits were taken to determine the number events a simulated data set required in order for the approximated $\mathcal{Z}$ distribution to produce dependable results. Using a simulated $4^+ \rightarrow 2^+ \rightarrow 0^+$ cascade with 10^9 events, a set of lower-statistics angular correlations were made by creating histograms filled with a smaller number of events using the same distribution found from the high-statistics histogram. For each histogram in this set, the calculated and measured angular correlations were extracted. Here, the ratio between the calculated and measured a_2 and a_4 coefficients was taken against the number of recorded coincidences, with the result shown in Figure 4.7. As this result shows, the ratio between $\tilde{a}_2$ and a_2 converges to 1.0233 ± 0.0006, while the ratio between $\tilde{a}_4$ and a_4 converges to 1.103 ± 0.006. The higher variance found in the calculated vs. measured a_4 coefficients can be attributed to the degree to which a_4 can be measured, due to its considerably smaller value to a_2, as well as the ability of the approximated $\mathcal{Z}$ to determine an accurate value of $\tilde{a}_4$ within a certain degree of error. Here, the limiting factor of the convergence is the error from the measured c_2 and c_4 coefficients needed to calculate $\tilde{a}_2$ and $\tilde{a}_4$. Given the dependence of the calculated a_4 on a_2 shown in Figure 4.4, and the variation seen for the a_4 coefficient in Figure 4.7, the effect of a_4 on the calculated angular coefficients needs to be explored further in order to quantify the limits to which the approximated $\mathcal{Z}$ distribution can be used given a desired level of error.
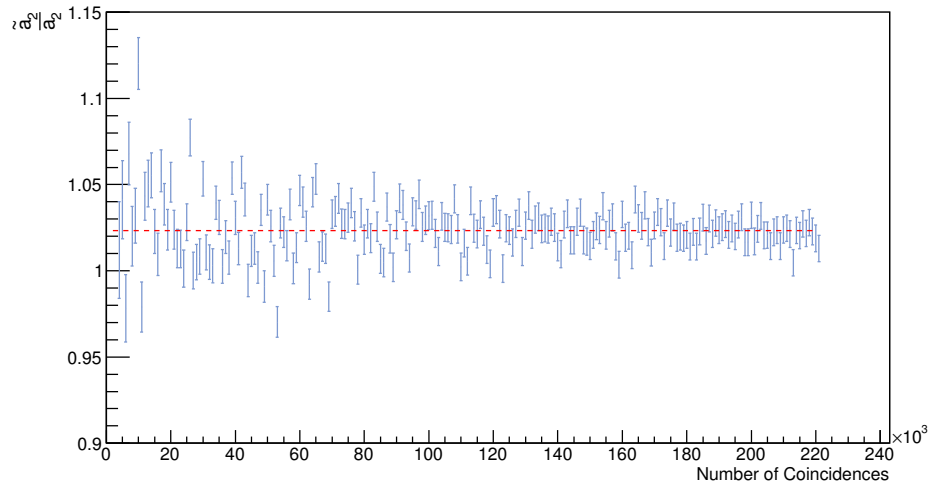
(a)
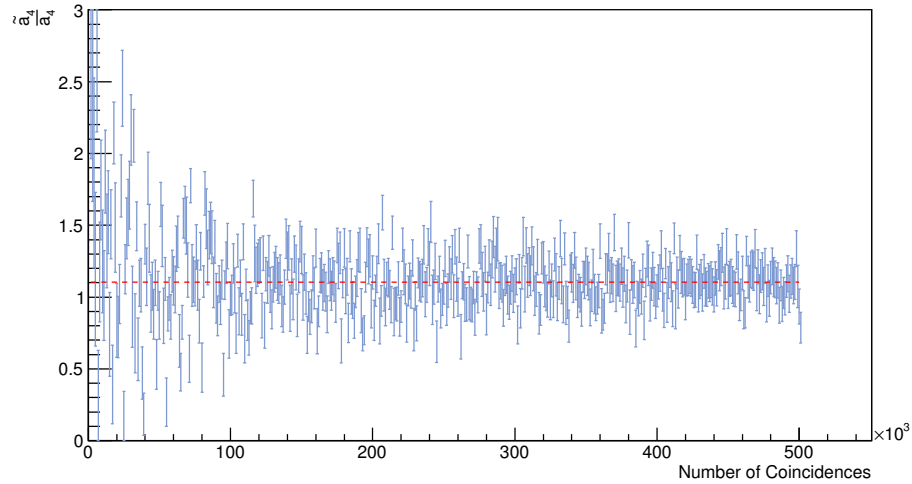
(b)

Figure 4.7: Convergence test result for the calculated against fitted angular coefficients for the $4^+ \rightarrow 2^+ \rightarrow 0^+$, with the number of coincidences recorded in the simulated data. (a) The ratio between $\tilde{a}_2$ and a_2 converges to 1.0233 ± 0.0006 as shown by the dashed, red line, while (b) the ratio between $\tilde{a}_4$ and a_4 converges to 1.103 ± 0.006.

Conclusions

The RS method was created in order to expedite the data analysis process for $\gamma - \gamma$ angular correlations. Using the previous method, goodness-of-fit tests were performed by first simulating individual angular correlations for a particular γ cascade, and then computing a reduced chi-square between the simulated and experimental data to determine the spins of the cascade levels. Because each simulation requires roughly 20 days of computational time, comparing a number of simulations to experimental data can quickly become a time consuming process. By defining the $\mathcal{Z}$ distribution, a linear combination of three high-statistics Legendre polynomial simulations, it was then shown that the RS method could accurately reproduce simulated angular correlations by scaling and adding the components of the $\mathcal{Z}$ distribution according to the physical angular correlation coefficients, a_2 and a_4, for a desired cascade. In turn, the $\mathcal{Z}$ distribution was demonstrated as being able to perform goodness-of-fit tests without the step of simulating each angular correlation to be compared to experiment - dramatically reducing the time needed to assign nuclear spin states.

Furthermore, the utility of the RS method was expanded by approximating the $\mathcal{Z}$ distribution as a linear combination of lines fit to each simulated component of the distribution. It was found that a set of algebraic expressions created from the approximation could not only analytically calculate the measured coefficients of a simulated angular correlation as a function of the physical coefficients a_2 and a_4 , but could also calculate the physical coefficients of an angular correlation as a function of the measured coefficients. The implications of the latter calculation suggest that experimentalists performing analysis on angular correlations could simply extract the measured angular correlation coefficients by fitting data with a line, and then calculate the adjusted coefficients that more closely agree with the physical values. By using the approximation, no fitting process would be required beyond that needed to create the approximation itself.

The methods developed in this thesis were tested on simulated angular correlations for different cascades of ^{60}Co decay. For the validity of both the RS method and

its approximation to be fully verified, the next step would need to be testing both methods using real experimental data from the GRIFFIN spectrometer and benchmarking it against the results from using simulation. Additionally, as only the decay of ^{60}Co was studied, the γ-ray energies for all simulated cascades were limited to 1173 and 1332 keV. Performing analysis on different cascades at varying energies would not only add depth to the validation of both methods, but could also come to prove the energy independence of the $\mathcal{Z}$ distribution, should the distribution remain constant being simulated using different energies. If energy independence is able to be shown, then the $\mathcal{Z}$ distribution would not need to be re-simulated between different cascades and would thus only need to be created once.
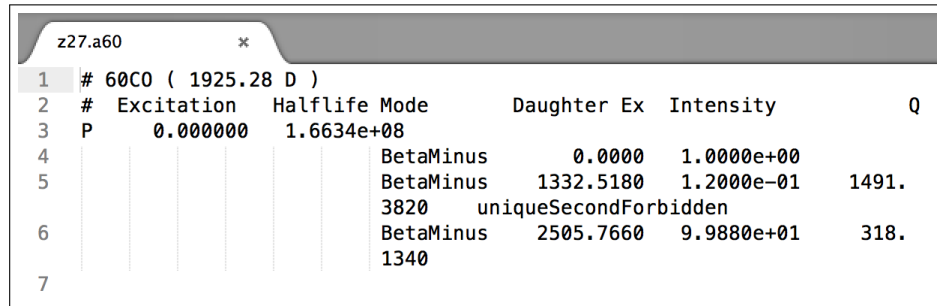
Appendix A

Simulation Reference

Once the GGAC Geant4 extension is installed, it can be tested using the `rdecay01` example simulation found in the installation package. In order to run any Geant4 simulation through the command line, a macro file containing appropriate commands is needed. The macro used for the example–`Co60.mac`–allows for a user to define the properties of the ^{60}Co decay by directing the simulation to data files containing the relevant decay information. For ^{60}Co, these are the radioactive decay and photon evaporation files, which are found in the following Geant4 directories:

```
/usr/local/geant4.10.01/share/Geant4-10.1.0/...
data/RadioactiveDecay4.2/z27.a60
```

```
/usr/local/geant4.10.01/share/Geant4-10.1.0/...
data/PhotonEvaporation3.1/z28.a60
```
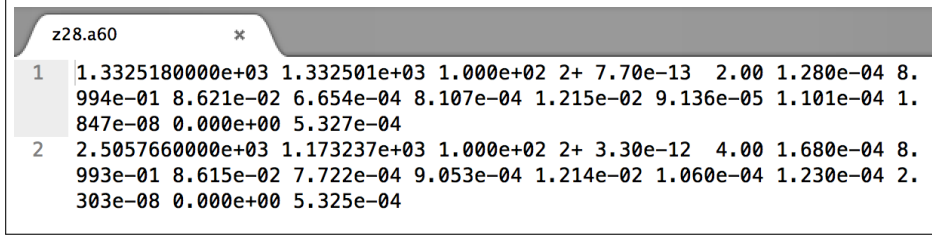
To simulate a ^{60}Co decay with a single β^- decay and two γ decays, the files were modified to look like the following:


```
z27.a60                      ✕
1  # 60CO ( 1925.28 D )
2  #  Excitation   Halflife Mode        Daughter Ex  Intensity           Q
3  P     0.000000   1.6634e+08
4                              BetaMinus        0.0000   1.0000e+00
5                              BetaMinus     1332.5180   1.2000e-01    1491.
   3820    uniqueSecondForbidden
6                              BetaMinus     2505.7660   9.9880e+01     318.
   1340
7
```

Figure A.1: Radioactive decay file for ^{60}Co

Note that we want the photon evaporation file to be for the ground state nucleus ^{60}Ni. In the macro file, the input commands for the files are:

```
 z28.a60                    ✕
 1   1.3325180000e+03 1.332501e+03 1.000e+02 2+ 7.70e-13  2.00 1.280e-04 8.
     994e-01 8.621e-02 6.654e-04 8.107e-04 1.215e-02 9.136e-05 1.101e-04 1.
     847e-08 0.000e+00 5.327e-04
 2   2.5057660000e+03 1.173237e+03 1.000e+02 2+ 3.30e-12  4.00 1.680e-04 8.
     993e-01 8.615e-02 7.722e-04 9.053e-04 1.214e-02 1.060e-04 1.230e-04 2.
     303e-08 0.000e+00 5.325e-04
```

Figure A.2: Photon evaporation file for ^{60}Ni

```
/grdm/setRadioactiveDecayFile 27 60 modified_z27.a60
/grdm/setPhotoEvaporationFile 28 60 modified_z28.a60
```
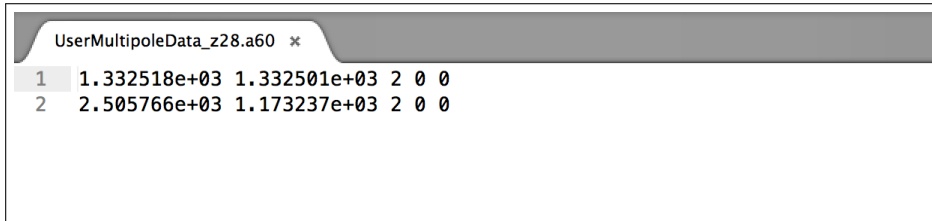
which include the Z and the A of the nucleus. With the file locations specified, a normal radioactive decay simulation was run using the using the shell command:

```
$ rdecay01 Co60.mac
```

To run the GGAC package, the multipole file was first created. The file was formatted to have five columns and a row for each γ ray emitted in the decay. The first column is the level energy and the second column is the γ ray energy, with both columns being identical to the first two found in the photon evaporation file. The next three columns describe the multipolarity of the transition – L_1 and L_2 – and the mixing ratio, where

$$\delta = \frac{L_2}{L_1}. \tag{A.1}$$

For two pure E2 transitions from $4^+ \rightarrow 2^+ \rightarrow 0^+$, the multipole file is written as:

```
 UserMultipoleData_z28.a60  ✕
 1   1.332518e+03 1.332501e+03 2 0 0
 2   2.505766e+03 1.173237e+03 2 0 0
```

Figure A.3: Multipole file for ^{60}Ni

The GGAC extension also requires a command for the spin of the ground state of the daughter nucleus. To incorporate the GGAC inputs into the radioactive decay simulation, the following commands were added to the run macro:

```
/grdm/setMultipoleFile 28 60 multipole_file
/grdm/setMultipoleGroundStateSpinAngularMomentum 28 60 0.0
```

Once the macro was edited to include the GGAC inputs, a test simulation was run to ensure the simulation package was producing angular correlations in an empty Geant4 space.

The Geant4 simulation code for the GRIFFIN geometry was then installed as an additional package to the Geant4 source code. Once the GGAC test simulations were completed and were shown to produce an angular correlation with the added multipole file, simulations were then run under the detector geometry. The macro file used for the GRIFFIN Co60 decay simulations allows for the control of the specific detector properties, and takes the same user defined radioactive decay files as the test simulations did. The shell command for this is

```
$ Griffinv10 60Co.mac
```

and should be done under the build directory for the detector simulations.

The root file produced from a GRIFFIN decay simulation contains an Ntuple: a data tree of information about simulated events such as crystal energy and time. In order to convert this data into more appropriate forms (histograms, matrices, etc.), the output is fed into a program called NTuple. NTuple takes two files, the Geant4 output and a settings file, and returns a root file containing histograms:

```
$ NTuple -sf Settings.dat -if g4out.root -of your_name_here.root
```

`Settings.dat` specifies the resolution and energy thresholds for each detector crystal, in addition to the types of histograms to be produced. For the simulations used in this thesis, the settings file was written to create only multidimensional histograms with 150 bins and a threshold of 1500 keV.

A.1 Simulating $\mathcal{Z}$ distributions

In order to simulate the Z_0, Z_2, and Z_4 distributions, the GGAC extension to Geant4 was edited to overwrite the automatic creation of angular correlation coefficients and manually set the values of a_2 and a_4. This override of coefficients was written as an extension of GGAC, and needs only one additional command in the simulation macro. The command is the following:

```
/grdm/setAngularCorrelationCoefficients 0.0 1.0 0.0
```

where the three input values correspond to a_2, a_4, and a_6. For example, if the simulation is run with the above command, a_4 will be set to 1 and the $Z_4(\theta)$ distribution will be created.

Appendix B

Supplemental Algebra

The $\mathcal{Z}$ distribution is approximated by first re-defining the three individual distributions as separate $W(\theta)$ functions:

$$\mathcal{Z}_0 \to \mathcal{L}_0 = \alpha_0(1 + \alpha_2 P_2 + \alpha_4 P_4)$$
$$\mathcal{Z}_2 \to \mathcal{L}_2 = \beta_0(1 + \beta_2 P_2 + \beta_4 P_4) \tag{B.1}$$
$$\mathcal{Z}_4 \to \mathcal{L}_4 = \gamma_0(1 + \gamma_2 P_2 + \gamma_4 P_4),$$

with α, β, and γ being the coefficients that delineate each function, respectively. As was described in Chapter 3, the $\mathcal{Z}$ distribution is created from a linear combination of the individual distributions using the physical a_2 and a_4 coefficients (Equation 3.9). Using the approximated $\mathcal{L}$ distributions, the $\mathcal{Z}$ distribution then becomes:

$$\mathcal{Z} \approx (1 - a_2 - a_4)\mathcal{L}_0 + a_2\mathcal{L}_2 + a_4\mathcal{L}_4$$

$$= (1 - a_2 - a_4)[\alpha_0(1 + \alpha_2 P_2 + \alpha_4 P_4)] + a_2[\beta_0(1 + \beta_2 P_2 + \beta_4 P_4)] + a_4[\gamma_0(1 + \gamma_2 P_2 + \gamma_4 P_4)]$$

$$= N[(1 - a_2 - a_4)(1 + \alpha_2 P_2 + \alpha_4 P_4) + a_2(1 + \beta_2 P_2 + \beta_4 P_4) + a_4(1 + \gamma_2 P_2 + \gamma_4 P_4)] \tag{B.2}$$

Here, it becomes important to note that the normalization coefficients - α_0, β_0, and γ_0 - are roughly equal to one another, as shown in Table 4.1. This equivalence allows for a simplification of the approximation of $\mathcal{Z}$, where N is defined to be $\alpha_0 = \beta_0 = \gamma_0$.

Continuing the approximation, where:

$$\mathcal{Z} \approx N[1 + (\alpha_2 - a_2\alpha_2 - a_4\alpha_2 + a_2\beta_2 + a_4\gamma_2)P_2 + (\alpha_4 - a_2\alpha_4 - a_4\alpha_4 + a_2\beta_4 + a_4\gamma_4)P_4]$$

$$\equiv N[1 + c_2 P_2 + c_4 P_4],$$

(B.3)

for

$$c_2 = \alpha_2 - a_2(\alpha_2 - \beta_2) - a_4(\alpha_2 - \gamma_2),$$

(B.4)

and

$$c_4 = \alpha_4 - a_2(\alpha_4 - \beta_4) - a_4(\alpha_4 - \gamma_4).$$

(B.5)

The coefficients c_2 and c_4 then give us the system of linear equations:

$$a_2(\alpha_2 - \beta_2) + a_4(\alpha_2 - \gamma_2) + (c_2 - \alpha_2) = 0$$

(B.6)

$$a_2(\alpha_4 - \beta_4) + a_4(\alpha_4 - \gamma_4) + (c_4 - \alpha_4) = 0.$$

(B.7)

By solving for a_4 in the Equation B.6, where

$$a_4 = \frac{-a_2(\alpha_2 - \beta_2) - (c_2 - \alpha_2)}{\alpha_2 - \gamma_2},$$

(B.8)

we can solve for a_2 in Equation B.7.

$$a_2(\alpha_4 - \beta_4) + \frac{-a_2(\alpha_2 - \beta_2) - (c_2 - \alpha_2)}{\alpha_2 - \gamma_2}(\alpha_2 - \gamma_4) + (c_4 - \alpha_4) = 0$$

$$a_2(\alpha_4 - \beta_4) - \left[\frac{a_2(\alpha_2 - \beta_2)}{\alpha_2 - \gamma_2} - \frac{c_2 - \alpha_2}{\alpha_2 - \gamma_2}\right](\alpha_4 - \gamma_4) = -c_4 + \alpha_4$$

$$a_2(\alpha_4 - \beta_4) - a_2\frac{(\alpha_2 - \beta_2)(\alpha_4 - \gamma_4)}{\alpha_2 - \gamma_2} = -c_4 + \alpha_4 + \frac{(c_2 - \alpha_2)(\alpha_4 - \gamma_4)}{\alpha_2 - \gamma_2}$$

(B.9)

$$a_2\left[\alpha_4 - \beta_4 - \frac{(\alpha_2 - \beta_2)(\alpha_4 - \gamma_4)}{\alpha_2 - \gamma_2}\right] = -c_4 + \alpha_4 + \frac{(c_2 - \alpha_2)(\alpha_4 - \gamma_4)}{\alpha_2 - \gamma_2}$$

$$a_2 = \left[-c_4 + \alpha_4 + \frac{(c_2 - \alpha_2)(\alpha_4 - \gamma_4)}{\alpha_2 - \gamma_2}\right]\left[\alpha_4 - \beta_4 - \frac{(\alpha_2 - \beta_2)(\alpha_4 - \gamma_4)}{\alpha_2 - \gamma_2}\right]^{-1}.$$

Similarly, by solving for a_2 in Equation B.6, with

$$a_2 = \frac{-a_4(\alpha_2 - \gamma_2) - (c_2 - \alpha_2)}{\alpha_2 - \beta_2}, \tag{B.10}$$

we can solve for a_4 in Equation B.7:

$$\frac{-a_4(\alpha_2 - \gamma_2) - (c_2 - \alpha_2)}{\alpha_2 - \beta_2}(\alpha_4 - \beta_4) + a_4(\alpha_4 - \gamma_4) + (c_4 - \alpha_4) = 0$$

$$\left[\frac{-a_4(\alpha_2 - \gamma_2)}{\alpha_2 - \beta_2} - \frac{c_2 - \alpha_2}{\alpha_2 - \beta_2}\right](\alpha_4 - \beta_4) + a_4(\alpha_4 - \gamma_4) = -c_4 + \alpha_4$$

$$-a_4\frac{(\alpha_2 - \gamma_2)(\alpha_4 - \beta_4)}{\alpha_2 - \beta_2} + a_4(\alpha_4 - \gamma_4) = -c_4 + \alpha_4 + \frac{(c_2 - \alpha_2)(\alpha_4 - \beta_4)}{\alpha_2 - \beta_2} \tag{B.11}$$

$$a_4\left[\alpha_4 - \gamma_4 - \frac{(\alpha_2 - \gamma_2)(\alpha_4 - \beta_4)}{\alpha_2 - \beta_2}\right] = -c_4 + \alpha_4 + \frac{(c_2 - \alpha_2)(\alpha_4 - \beta_4)}{\alpha_2 - \beta_2}$$

$$a_4 = \left[-c_4 + \alpha_4 + \frac{(c_2 - \alpha_2)(\alpha_4 - \beta_4)}{\alpha_2 - \beta_2}\right]\left[\alpha_4 - \gamma_4 - \frac{(\alpha_2 - \gamma_2)(\alpha_4 - \beta_4)}{\alpha_2 - \beta_2}\right]^{-1}.$$

References

[1] J. M. Blatt and V. F. Weisskopf. *Theoretical Nuclear Physics*. John Wiley & Sons, 4th edition, 1991.

[2] IAEA Nuclear Data. Live chart of nuclides. URL `https://www-nds.iaea.org/relnsd/vcharthtml/VChartHTML.html`.

[3] S.J. Robinson. *Nuclear Instruments and Methods in Physics Research*, A292: 386–400, 1990.

[4] A. Perez-Andujar and L. Pibida. Performance of cdte, hpge and nai(tl) detectors for radioactivity measurements. *Applied Radiation and Isotopes*, 2004.

[5] Ryan Dunlop. High-precision branching ratio measurement for the superallowed + emitter 74rb. Master's thesis, University of Guelph, 2012.

[6] Andrew MacLean. Gamma-gamma angular correlation measurements with griffin. Master's thesis, University of Guelph, 2016.

[7] Stable isotopes of the elements. URL `http://www.periodictable.com/Properties/A/StableIsotopes.html`.

[8] David Griffiths. *Introduction to Quantum Mechanics*. Pearson Prentice Hall, 2nd edition, 2004.

[9] Carlos Bertulani. *Nuclear Physics in a Nutshell*. Princeton University Press, 2007.

[10] K. Heyde. *Basic Ideas and Concepts in Nuclear Physics*. Institute of Physics Publishing, 3rd ed edition, 2004.

[11] Chapter 10: Nuclear properties. University of Michigan, 2015.

[12] K. Krane. *Introduction to Nuclear Physics*. Wiley, 3rd edition, 1987.

[13] M.G. Bowler. *Nuclear Physics*. Oxford, 1973.

[14] B. Alex Brown. Lecture notes in nuclear structure physics, November 2005 2005.

[15] D. Williams. *Methods of Experimental Physics*. Academic Press Inc., 1976.

[16] H. Frauenfelder and S. R. M. *Alpha-, Beta-, and Gamma-Ray Spectroscopy.* North-Holland Publishing Company, 5th edition, 1979.

[17] G.F. Knoll. *Radiation Detection and Measurement.* John Wiley & Sons, Inc., 3rd edition, 2000.

[18] R. D. Evans. *The Atomic Nucleus*. 1982.

[19] UCSD. Compton scattering. URL `http://quantummechanics.ucsd.edu/ph130a/130_notes/node59.html`.

[20] W.R. Leo. *Techniques for Nuclear and Particle Physics Experiments.* SpringerVerlag, 2nd edition, 1994.

[21] R.D. Evans. *The Atomic Nucleus*. Krieger, 1982.

[22] Los Alamos National Laboratory. Gamma-ray interactions with matter. Online.

[23] C. E. Svensson and A. B. Garnsworthy. The griffin spectrometer. *Hyperfine Interactions*, 225:127–132, 2014.

[24] TRIUMF. Isac facilities for rare-isotope beams. URL `http://www.triumf.ca/research-program/research-facilities/isac-facilities`.

[25] Griffin Collaboration. Hardware, . URL `http://griffincollaboration.github.io/griffin-website/hardware.html#hpge`.

[26] A.B. Garnsworthy et al. U. Rizwan. Characteristics of griffin high-purity germanium clover detectors. *Nuclear Instruments and Methods in Physics Research*, A (820):126–131, 2016.

[27] Griffin Collaboration. Data acquisition, . URL `http://griffincollaboration.github.io/griffin-website/daq.html`.

[28] S. Agostinelli et al. Geant4—a simulation toolkit. *Nuclear Instruments and Methods in Physics Research*, 506:250, 2003.

[29] Evan Rand. Geant4 gamma-gamma angular correlations (ggac). URL `https://github.com/GRIFFINCollaboration/Geant4GammaGammaAngularCorrelations10.01.p01`.

[30] Geant4 Collaboration. The radioactive decay module, . URL `http://geant4.cern.ch/G4UsersDocuments/UsersGuides/PhysicsReferenceManual/html/node180.html`.

[31] R. Avida et al. *Nuclear Instruments and Methods*, 46:350, 1966.

[32] J.K. Smith. Angular correlations. URL `https://github.com/GRIFFINCollaboration/GRSISort/wiki/Angular-Correlations`.

[33] M.E. Rose. *Multipole Fields*. New York: Wiley, 1955.

[34] The University of Guelph. Griffin. URL `https://www.physics.uoguelph.ca/Nucweb/griffin.html`.

[35] K. Heyde. *Basic Ideas and Concepts in Nuclear Physics*, volume 3rd ed. Institute of Physics Publishing, 2004.